U. Walzer, R. Hendel, and J. Baumgardner. Viscosity stratification and a 3D compressible spherical shell model of mantle evolution. In E. Krause, W. Jäger, and M. Resch, editors, High Perf. Comp. Sci. Engng. '03, pages 27-67. Berlin, 2004b.

Viscosity stratification and a 3-D compressible spherical shell model of mantle evolution

Uwe Walzer[1], Roland Hendel[1], and John Baumgardner[2]

[1] Institut für Geowissenschaften, Friedrich-Schiller-Universität, Burgweg 11, 07749 Jena, Germany
[2] Los Alamos National Laboratory, MS B216 T-3, Los Alamos, NM 87545, USA

Abstract. The viscosity stratification has a strong influence on the thermal *evolution* of a compressible Earth's mantle with time-dependent internal heating. The differential equations for infinite Prandtl-number convection are solved using a three-dimensional finite-element spherical-shell method on a computational mesh derived from a regular icosahedron with 1.351.746 or, alternatively, 10.649.730 nodes. We formulate a radial viscosity profile from solid-state physics considerations using the seismic model PREM. New features of this viscosity profile are a *high-viscosity transition layer* beneath the usual asthenosphere, a *second low-viscosity layer* below the 660-km endothermic phase boundary and a considerable *viscosity increase* in the lower 80 % of the lower mantle. To be independent of the special assumptions of this derivation, we vary the level and the form of this profile as well as the other physical parameters in order to study their consequences on the planforms and on the convection mechanism. The effects of the two mineral phase boundaries at 410 and 660 km depth proved to be smaller than effects of the strong variation of viscosity with radius. The latter had more influence on the convective style than all other parameters. Values of our material parameters are time independent and constant in the lateral directions, except for viscosity.
The focus of this paper is a variation of non-dimensional numbers as Rayleigh number, *Ra*, Nusselt number, *Nu*, the reciprocal value, *Ror*, of the Urey number, viscosity-level parameter, r_n, etc. We explored the parameter range for special solutions. For the wide parameter range $-0.5 \leq r_n \leq +0.3$, that includes our preferred viscosity profile, we obtain solutions characterized by reticular connected *thin cold sheet-like downwellings*. The downwellings are thinner than similar features in previous publications. They bear a resemblance to observed subducting slabs but are purely vertical. We find it remarkable that the downwellings penetrate the high-viscosity transition layer. They remain sheet-like to 1350 km depth. Below this depth they begin to lose definition but their locations are still visible at 1550 km depth. Such thin

subducting sheets are notable since the viscosity is Newtonian. On the other hand, it is not surprising there are no transform-like features at the surface of the model. We compute laterally averaged heat flow at the Earth's surface, the ratio of heat output to radiogenic heat production, *Ror*, the Rayleigh number and the Nusselt number as a function of time. $Nu_{(2)}$ denotes the temporal average of the Nusselt number of a run for the last 2000 Ma of the evolution, $Ra_{(2)}$ is the temporal average of the Rayleigh number, respectively. For a wide parameter range, we obtain $Nu_{(2)} = 0.120\ Ra_{(2)}^{0.295}$ in this model.

1 Introduction

The focus of this paper is a parameter variation of the radial viscosity profile of the Earth's mantle and a variation of non-dimensional numbers that characterize thermal convection. The patterns of the planforms are relevant, too. We take an interest not only in convection of the geological present but also in the evolution of relevant parameters, e.g. Nusselt number and Urey number, as a function of time in the past.
For reasons explained in Section 3.4, we assume that the segregation of the metallic core and the primordial silicate mantle was finished $(4.49 \pm 0.03) \times 10^9$ a ago. The present model is essentially a viscous spherical shell heated mainly by radioactive decay from within and, only to a minor degree, from below. The spherical shell had a primordial initial heat and cooled down the course of the thermal evolution. For geochemical reasons, the start of the evolution of the system was fixed for an age of 4.49 Ga. In spite of this and other geochemical and geophysical specifications of the model, we are of course not able to model the Earth's mantle in a self-consistent manner, taking into account all the complexities necessary. E.g., it is not the focus of this paper to contribute to the problem of self-consistent generation of oceanic lithospheric plates (Bercovici, 1996; Christensen, 1996; Trompert and Hansen, 1998; Tackley, 2000a, 2000b, 2001, Bercovici et al., 2001a; etc.). Furthermore, the mantle of the model is chemically homogeneous. It contains no chemically different reservoirs. At the upper surface, there are no continents that would be able to modify the upper boundary conditions. Therefore the model is heated, spatially homogeneously and temporally decaying, essentially from within supposing the abundances of McCulloch and Bennett (1994) that do not essentially deviate from the primordial mantle abundances of Hofmann (1988). Although we fix further quantities and incorporate the two major mineral phase transitions into the model, we are able to characterize the essential features of the evolution of the system by a few non-dimensional numbers as the Rayleigh number, *Ra*, the Nusselt number, *Nu*, the reciprocal value, *Ror*, of the Urey number, the non-dimensional viscosity-level number, r_n, etc. We varied the mentioned numbers since many geophysical properties are not well constrained. The variation of the mantle's viscosity has the largest effect on the mechanism and on the non-dimensional numbers. Therefore, this varia-

tion is the center of this paper. Of course, the results directly refer only to the mechanism of the model and not immediately to the real mantle. Every geodynamical model can be criticized from two flanks. Firstly, it is feasible to refer to some non-included feature of the real mantle. In our model, e.g., volatiles are not explicitly included. In this case, a critical reader could demand a more complex model. On the other hand, another reader could require a simplification to allow that new understanding of fluid dynamics comes out of this paper. So, we would learn to understand each single mechanism. But unfortunately, a linear superposition of solutions is not possible since the equations are nonlinear. Therefore, it is legitimate to find a geophysical compromise between the two mentioned contradictory demands, provided that we can grasp the essence by non-dimensional numbers etc. The usual survey of related evolution and convection models occurs in Section 5.

2 Viscosity. General considerations

So far, the public discussion of the influence of viscosity on mantle convection was concentrated on temperature dependence. As is well known, Bénard convection in a constant viscosity fluid layer can be parameterized by the Nusselt number and the Rayleigh number only. If, additionally, the temperature dependence is taken into account then further parameters have to be introduced. If we have the simple expression

$$\eta = \eta_{ref} \cdot exp[-E(T - T_{ref})] \tag{1}$$

then a further non-dimensional number, r_η, has to be introduced where

$$r_\eta = exp(E \cdot \Delta T) \tag{2}$$

η is viscosity, η_{ref} is reference viscosity, E is a constant, T is temperature, T_{ref} is reference temperature, r_η is a viscosity ratio, and ΔT is the fixed total temperature difference across the fluid layer. In this simple case, convection is in the small viscosity contrast regime for $r_\eta \leq 10^2$, in the sluggish-lid regime for $10^2 < r_\eta < 10^4$, and in the stagnant-lid regime for $r_\eta \geq 10^4$ (Christensen, 1985, Solomatov, 1995, Reese et al., 1998, 1999, Schubert et al., 2001). The viscosity between the two thermal boundary layers is nearly constant. If it is intended to apply such simple temperature-dependent viscosity convection models to the mantle then we raise three principal objections to the effect that corresponding supplementations are necessary:
a) Viscosity is also pressure-dependent. In particular for minerals of the lower mantle, the rising pressure causes a strongly increasing viscosity. Even if the lower-mantle composition would not depend on depth, the product of activation volume and pressure generates a strong viscosity increase with depth, without jumps, so that the temperature effect is overcompensated except perhaps for D″ and plumes.

b) It is an obvious assumption that not only density, compressional velocity and shear velocity jump at the major phase boundaries of the mantle but also activation energy and activation volume of the relevant creeping mechanism (Karato et al., 1995, Karato, 1997a, Ranalli, 1998). Since the activation enthalpy is in the exponent of the viscosity equation, major viscosity jumps are to be expected. We will show that the influences of a) and b) on the planforms are essential.
c) We take an interest not only in mantle convection of a short time interval but also in the thermal evolution all the 4490 Ma round. Based on geological observations, it is a realistic approach to assume a constant upper surface temperature. However, there are good reasons and observations to assume that the volumetrically averaged temperature, T_a, of the mantle diminishes as a function of time. Therefore, the temperature at the core-mantle boundary (CMB) is probably *not* a constant *with respect to time*. For *evolution* models, the difference ΔT cannot be a constant. This conclusion applies equally to viscous layer models and spherical shell models. Further arguments are given in Section 3.4.

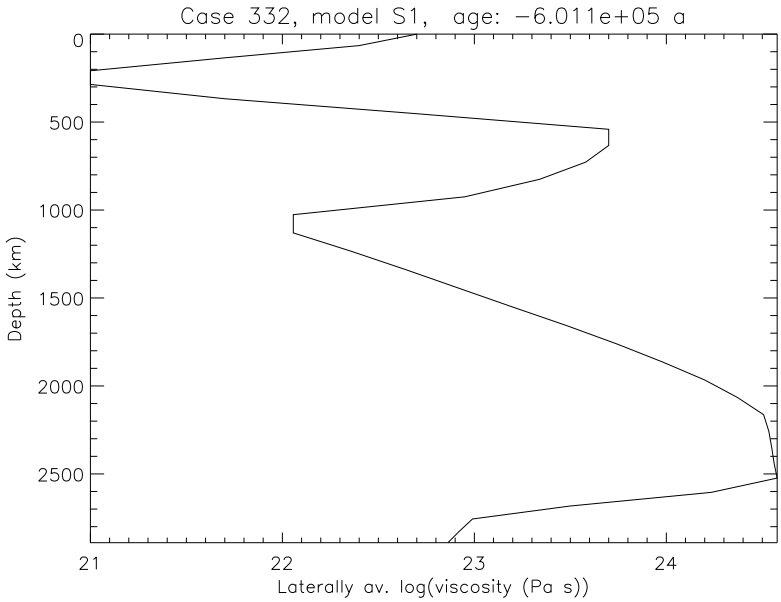

Fig. 1. The basic radial viscosity profile, $\eta_1(r)$ for $r_n = 0$.

Because of a) and b) we offer now a survey of possible radial viscosity profiles for the Earth's mantle. We then present the reasons for the viscosity profile, we favor most, as shown in Fig. 1 and specified by Eq. (5). It is this profile we than apply in our three-dimensional thermal evolution model of the mantle.

Starting from this preferred viscosity distribution, we vary our parameters to learn the range of validity of the corresponding numerical solutions. Increasing pressure reduces the number of defects, but increasing temperature generates an increased number of defects and dislocations. The change in viscosity with pressure is due not only to the number of defects or dislocations, but also to the change in their mobility, i.e., the energy required to jump from one site to another increases with pressure. Therefore, the solid-state viscosity increases with increasing pressure and decreases with increasing temperature. Because the P, T-dependence of the other physical parameters is much smaller, we assume only a radial dependence in these other quantities.

Unfortunately, the viscosity of the mantle is relatively poorly constrained. There are two classes of methods for estimating mantle viscosity as a function of depth. The *first* class of methods relies upon geophysical observables such as post-glacial rebound data, the geoid, global seismic tomography models, and observed surface heat flow. The *second* class relies upon physical investigations of the creep mechanisms in monocrystalline and polycrystalline silicates and oxides at high pressure and high temperature. The *first* class is exemplified by investigations that derive depth-dependent mantle viscosity from deformation of spherical-earth models by surface loads, e.g., by a changing ice-water distribution (Lambeck and Johnston, 1998). In addition there are anelastically compressible internal loading theories. Tomography derived differences in the seismic compressional wave velocity, v_p, and the seismic shear wave velocity, v_s, can be converted into density differences using an empirical relation. The observed aspherical geoid anomalies as well as the observed free-air gravity field ought to be identical to the corresponding theoretical quantities arising from such density differences. Such studies typically assume mantle convection is driven by density differences derived from the tomography. In a convecting mantle, the actual geoid depends not only on the density heterogeneity but also on the mantle's viscosity structure. Typically, however, calculations of this sort that seek to recover the mantle's viscosity structure have yielded wildly different viscosity distributions as a function of depth. Various alternatives have been explored to reduce this ambiguity. Pari and Peltier (1998), for example, sought to mitigate the extreme degree of nonuniqueness by constraining the radial component of the internal-load driven flow velocity to be linearly related to the surface heat flow.

In the seismic velocity-to-density scaling it is usually assumed that the seismic velocity anomalies have a thermal origin. Since this premise is clearly wrong for the continental lithospheric mantle and partly wrong for subducted oceanic slabs, Kido and Čadek (1997) restricted this procedure to only the *oceanic* geoid at intermediate degrees *(l= 12–15)* and to areas at a sufficiently large distance from slabs. As a starting point, they explored three different seismic tomography models and five rather different radial profiles for the velocity-to-density scaling factors $(\partial \ln \rho / \partial \ln v_p)$ and $(\partial \ln \rho / \partial \ln v_s)$. Their inversion technique sought to maximize the correlation between observed and predicted oceanic geoid at degrees 12–25. Kido and Čadek (1997) used a ge-

netic algorithm to find the maximum correlation coefficient. They found *two* low-viscosity layers from their inversions for *all* 15 combinations of the three seismic tomography models and the five velocity-to-density scaling profiles. One of these layers was the usual asthenosphere immediately beneath the lithosphere, while the other one was situated within the upper quarter of the lower mantle.

We suggest that the most likely profiles have a second low viscosity layer that begins *immediately* beneath the 660-km phase boundary since the activation energy and the activation volume of the relevant minerals must jump at the phase boundary independent of the prevailing creeping mechanism. Moreover, the grain-size reduction of material flowing downward through the 660-km boundary is a good argument in favor of a second low-viscosity layer just below the 660 (Kubo et al., 2000). Čadek and van den Berg (1998) discussed a parameterization of the radial temperature profile of the mantle where the geoid and the seismic velocities have been taken as observables. The well-known non-unique nature of the geoid inversions leads to two different sets of viscosity profiles. The first set, called A,B, has a stiff lithosphere at the top that is underlaid by a thick asthenosphere between 100 and 400 km depth and a viscosity maximum around 500 km depth. The next layers consist of a narrow low-viscosity zone *above* the 660-km discontinuity and a uniformly high viscosity through most of lower mantle. Only near the CMB does the viscosity decrease. A second set of viscosity profiles, called C,D, also display a stiff lithospheric lid. Beneath this lid is a flat viscosity minimum down to 660 km. At 660 km depth, the viscosity increases abruptly by 2-3 orders of magnitude followed by a second low-viscosity layer between 800 and 1000 km depth. A remarkable feature of the C,D viscosity profile is a broad viscosity maximum between 2000 and 2500 km depth. Finally, as in the A,B case, the viscosity decreases near the CMB.

A *second* class of methods for constraining the mantle's viscosity profile comes from mineral physics. Based on broad consensus, Ranalli (1998) concluded that the rheology of the asthenosphere between 100 and 410 km depth is determined primarily by the creep properties of olivine, that of the transition layer primarily by the creep properties of spinel and garnet phases, and that of the lower mantle primarily by the properties of perovskite. If there is no drastic reduction in grain size within the transition layer, the creep properties of spinel and garnet appear to exclude low viscosity in this zone. Therefore we conclude the A,B set of viscosity profiles by Čadek and van den Berg (1998) must be excluded because of their narrow low-viscosity layer *above* the 660-km discontinuity. The main features of the C,D profiles seem more probable than those of the A,B profiles since solid-state physics considerations argue for a broad viscosity maximum in the lowermost 1000 km of the mantle apart from the D″ layer. For each of the different creep mechanisms, Ranalli (1998) specified values for the activation energy, E_0, and the activation volume, V_0. Even if some details are uncertain, it is evident that the viscosity must show *considerable jumps* at the phase boundaries in 410, 520, and 660 km of depth

since E_0 and V_0 are in the exponent of the function that describes the P,T-dependence of the viscosity.
Karato (1997a) emphasizes that garnet has a unique crystal structure that does not allow easy dislocation glide. An increase in density and seismic wave velocities does not mean that the viscosity continuously rises with depth since the resistance to plastic deformation in garnets is considerably higher than that of perovskite, olivine, spinel and most of the remaining mantle minerals. Karato et al. (1995) studied the deformation properties of both oxide and silicate garnets from room temperature up to $T = 0.95\ T_m$, where T_m denotes the melting temperature. They used an analogue materials approach to search for systematics since majorite is stable only at very high pressures. In their indirect approach, they used uvarovite, spessartine, grossular and some other garnets that belong to the same isomechanical group. All samples had high strength both at high temperatures (creep) and at low temperature (hardness). Karato et al. (1995) concluded that "the difference in creep strength between garnet and olivine compared at the same T/T_m is about a factor of 10, which would translate into a difference in diffusion coefficient of a factor of $\sim 10^3$, if creep were diffusion controlled." A similar statement applies for the comparison between majorite and perovskite.
This is one of the reasons why we introduced the radius-dependent part of the viscosity in the upper half of the mantle as shown in Fig. 1. For the lower part of the mantle, for depths between 1234.4 and 2891 km, we assume that perovskite controls the shear creeping and that the activation enthalpy can be estimated using the pressure dependence of the melting temperature of perovskite according to Zerr and Boehler (1993, 1994). Of course, we are conscious of the fact that the viscosity should jump abruptly at 410, 520 and 660 km depth. However, to avoid numerical difficulties we smooth the viscosity at these discontinuities.
There are two reasons to conclude the existence of a high-viscosity transition layer. The *first* reason was discussed by Karato et al. (1995). If the upper mantle consists of pyrolite with 20-40 % garnet, then the garnet does *not* control the rheology. For a model with more than 50 % garnet, the garnet would cause a maximum of the effective viscosity in the transition layer. Already more than a decade ago, Ringwood (1990) concluded more than 90 % garnet should exist at the bottom of the transition layer. Weidner (2001) showed that the stress capacity of the majorite, pyrope, wadsleyite and ringwoodite of the transition layer is much higher than that of the olivine above and the MgO below of it. The possible influence of water on the viscosity of the transition layer is discussed by Karato(2003). A *second* reason for a high-viscosity transition layer is derived in Section 3.1.

3 Model

In the following, the parts of the present model are consecutively presented.

3.1 The viscosity of the model

In this Section, we treat only that aspects of viscosity which are necessary for computation. In Section 2 we have put forward an argument for viscosity jumps at the major phase transitions in the mantle. A reason for the assumption of a high-viscosity transition layer was introduced in a paper by Walzer and Hendel (2003). In that paper, the authors derived the viscosity as a function of depth based on a method independent of prior geophysical approaches and also independent of approaches based on the distribution of minerals in the mantle.

The authors started from a self-consistent theory using the Helmholtz free energy, an equation of state (EoS), the free-volume Grüneisen parameter and Lindemann's law. Viscosity is determined as a function of melting temperature obtained from Lindemann's law. Walzer and Hendel (2003) applied the Ullmann-Pan'kov EoS, whereas in the present paper we use the Birch-Murnaghan EoS. We note that Birch-Murnaghan is a special case of the Ullmann-Pan'kov for $K_0' = 4$, where K_0' is the pressure derivative of the zero pressure bulk modulus. To obtain the relative variation in radial viscosity distribution, Walzer and Hendel (2003) relied upon the pressure, P, the bulk modulus, K , and $\partial K/\partial P$ from PREM (Dziewonski and Anderson, 1981) that is derived from seismic observations. For the absolute scale of the viscosity profile, Walzer and Hendel (2003) used the standard postglacial-uplift viscosity of the asthenosphere beneath the continental lithosphere. Two important conclusions of Walzer and Hendel (2003) are that not only the asthenosphere, but also the upper part of the lower mantle, has low viscosity and that a high-viscosity transition layer tends to divide the mantle into two principal reservoirs relative to concentrations of incompatible elements and volatiles. The transition layer acts as a barrier, but a permeable one, to flow across the mantle.

In the present approach, we do not apply the values of P, K and $\partial K/\partial P$ directly from PREM but rather values that were first smoothed by means of the Birch-Murnaghan EoS (Cf. Fig.2). Of course, we do not smooth across the phase boundaries. Apart from this difference, in the present paper, we derive our radial viscosity profile for 0 to 1234.4 km depth using the method of Walzer and Hendel (2003). This procedure avoids complex assumptions regarding the depth distribution of mineral phases but nevertheless allows derivation of the viscosity from observables. For depths between 1234.4 km and 2891 km, we derive the radial viscosity profile from the melting curve of perovskite (Zerr and Boehler, 1993, 1994; Boehler 1997). The resulting profile is displayed in Fig. 1 where viscosity jumps at the phase boundaries have been replaced by steep viscosity gradients to avoid numerical difficulties in our convection code. The general form of the P,T-dependence of viscosity, η, is given by the following expression where the pressure dependence is hidden in the melting temperature, T_m.

$$\eta = A \cdot \exp\ (c \cdot T_m/T) \tag{3}$$

This relation is equivalent to

$$\eta = A \cdot \exp\left(c\frac{T_m}{T_{av}}\right) \cdot \exp\left[cT_m\left(\frac{1}{T} - \frac{1}{T_{av}}\right)\right] \tag{4}$$

where T_{av} is the laterally averaged temperature. The formula has been slightly simplified by interpreting the first two factors as the radial factor, $\eta_1(r)$, of the viscosity.

$$\eta(r,\theta,\phi,t) = 10^{r_n} \cdot \eta_1(r) \cdot \exp\left[c_t \cdot T_m(r) \cdot \left(\frac{1}{T(r,\theta,\phi,t)} - \frac{1}{T_{av}(r,t)}\right)\right] \tag{5}$$

where r is the radius, θ the colatitude, ϕ the longitude and t the time. The viscosity therefore depends on these four independent variables.
The introduction of the factor 10^{r_n} is a generalization of the equation. For our first estimate of the viscosity, $r_n = 0$ has been chosen. The variation of the non-dimensional parameter r_n generates a systematic shift of the viscosity level. In Section 4.4, the form of the initial radial viscosity profile has been additionally varied to be independent of the specific derivation of $\eta_1(r)$.

3.2 Conservation of mass, momentum and energy

The model is based on the numerical solution of the equations expressing conservation of mass, momentum, and energy. The equation describing the conservation of mass,

$$\frac{\partial\rho}{\partial t} + \bigtriangledown \cdot (\rho\vec{v}) = 0 \tag{6}$$

under the anelastic-liquid approximation (i.e., neglecting the $\frac{\partial\rho}{\partial t}$ term) simplifies to

$$\bigtriangledown \cdot \vec{v} = -\frac{1}{\rho}\vec{v} \cdot \bigtriangledown\rho \tag{7}$$

where ρ is density, t time, and $\vec{v}$ is velocity.
The conservation of momentum can be expressed by

$$\rho\left(\frac{\partial\vec{v}}{\partial t} + \vec{v} \cdot \bigtriangledown\vec{v}\right) = -\bigtriangledown P + \rho\vec{g} + \frac{\partial}{\partial x_k}\tau_{ik} \tag{8}$$

where P is the pressure, $\vec{g}$ is the gravity acceleration, and τ_{ik} is the deviatoric stress tensor. For spherical symmetry, we have $\vec{g} = -g\vec{e_r}$ and the hydrostatic pressure gradient may be written

$$-\frac{\partial P}{\partial r} = \rho g \tag{9}$$

By definition $K_S = -V\left(\frac{\partial P}{\partial V}\right)_S$ and $\frac{V}{V_0} = \frac{\rho_0}{\rho}$, where K_S is the adiabatic bulk modulus, Vvolume, S entropy, r the radial distance from the Earth's center. Hence

$$K_S = \rho \left(\frac{\partial P}{\partial \rho}\right)_S = \rho \left(\frac{\partial P}{\partial r}\right)_S \left(\frac{\partial r}{\partial \rho}\right)_S \tag{10}$$

Substituting Eq. (9) into Eq. (10) we obtain

$$\left(\frac{\partial \rho}{\partial r}\right)_S = \frac{-\rho^2 g}{K_S} \tag{11}$$

Upon neglecting horizontal spatial variations in ρ Eqs. (7) and (11) yield

$$\bigtriangledown \cdot \vec{v} = -\frac{1}{\rho}\vec{v} \cdot \bigtriangledown \rho \cong -\frac{1}{\rho} v_r \frac{\partial \rho}{\partial r} = \frac{\rho g v_r}{K_S} \tag{12}$$

It is well-known that

$$K_S = \frac{c_p}{c_v} K_T = (1 + \alpha \gamma_{th} T) K_T \tag{13}$$

where K_T is the isothermal bulk modulus, c_p the specific heat at constant pressure, c_v the specific heat at constant volume, α the coefficient of thermal expansion, γ_{th} the thermodynamic Grüneisen parameter and T the absolute temperature.
Eq. (8) can be rewritten as

$$\rho \frac{dv_i}{dt} = \rho g_i + \frac{\partial \sigma_{ki}}{\partial x_k} \tag{14}$$

Using this equation, the conservation of energy can be expressed as follows

$$\rho \frac{du}{dt} + \frac{\partial q_i}{\partial x_i} = \mathcal{Q} + \sigma_{ik} \dot{\varepsilon}_{ik} \tag{15}$$

where u is the specific internal energy, $\mathcal{Q}$ is the heat generation rate per unit volume; v_i, g_i, q_i, x_i, σ_{ik}, $\dot{\varepsilon}_{ik}$ are the components of velocity, gravity acceleration, heat flow density, location vector, stress tensor and strain-rate tensor, respectively.
Another formulation of Eq. (15) is

$$\rho \left[\frac{\partial}{\partial t} + \vec{v} \cdot \bigtriangledown\right] u = \bigtriangledown \cdot (k \bigtriangledown T) + \mathcal{Q} - P \bigtriangledown \cdot \vec{v} + 2W_D \tag{16}$$

where

$$2W_D = \sigma_{ik} \dot{\varepsilon}_{ik} + P \bigtriangledown \cdot \vec{v} \tag{17}$$

and

$$q_k = -k \frac{\partial T}{\partial x_k} \tag{18}$$

k is the thermal conductivity. Using

$$du = T\ ds - P\ dv \tag{19}$$

and

$$du = T\left(\frac{\partial s}{\partial T}\right)_P dT + T\left(\frac{\partial s}{\partial P}\right)_T dP - Pdv \tag{20}$$

we eliminate the specific internal energy in Eq. (16) and obtain the equation

$$\rho c_p \frac{dT}{dt} = \bigtriangledown \cdot (k \bigtriangledown T) + \mathcal{Q} + \alpha T \frac{dP}{dt} + 2W_D \tag{21}$$

since

$$c_p = T\left(\frac{\partial s}{\partial T}\right)_P \quad \text{and} \quad \left(\frac{\partial s}{\partial P}\right)_T = -\left(\frac{\partial v}{\partial T}\right)_P = -v\alpha \tag{22}$$

Here is s the specific entropy, v the specific volume, c_p the specific heat at constant pressure and α the coefficient of thermal expansion.
Next let us derive a less well known version of the conservation of energy equation: Eq. (16) is equivalent to

$$\rho\left(\frac{du}{dt} + P\frac{dv}{dt}\right) = \tau_{ik}\frac{\partial v_i}{\partial x_k} + \bigtriangledown \cdot (k \bigtriangledown T) + \mathcal{Q} \tag{23}$$

because of Eq. (7) and $\frac{1}{\rho} = v$.
Inserting Eq. (19) into Eq. (23), we obtain

$$\rho T\frac{ds}{dt} = \tau_{ik}\frac{\partial v_i}{\partial x_k} + \frac{\partial}{\partial x_j}\left(k\frac{\partial}{\partial x_j}T\right) + \mathcal{Q} \tag{24}$$

On the other hand,

$$ds = \left(\frac{\partial s}{\partial T}\right)_v dT + \left(\frac{\partial s}{\partial v}\right)_T dv \tag{25}$$

and

$$\left(\frac{\partial s}{\partial T}\right)_v = \frac{c_v}{T} \quad , \quad \left(\frac{\partial s}{\partial v}\right)_T = \alpha K_T \tag{26}$$

This implies

$$Tds = c_v dT + \alpha K_T T d\left(\frac{1}{\rho}\right) \tag{27}$$

or

$$Tds = c_v dT - \frac{c_v \gamma T}{\rho} d\rho \tag{28}$$

where

$$\gamma_{th} = \frac{\alpha K_T}{c_v \rho} \tag{29}$$

is the thermodynamic Grüneisen parameter.
Inserting Eq. (28) into Eq. (24) we obtain

$$\rho c_v \frac{dT}{dt} - c_v \gamma T \frac{d\rho}{dt} = \tau_{ik}\frac{\partial v_i}{\partial x_k} + \frac{\partial}{\partial x_j}\left(k\frac{\partial}{\partial x_j}T\right) + \mathcal{Q} \tag{30}$$

From Equations (6) and (30)

$$\rho c_v \frac{dT}{dt} = -\rho c_v \gamma T \frac{\partial v_j}{\partial x_j} + \tau_{ik} \frac{\partial v_i}{\partial x_k} + \frac{\partial}{\partial x_j}\left(k \frac{\partial}{\partial x_j} T\right) + \mathcal{Q} \tag{31}$$

or

$$\frac{\partial T}{dt} = -v_j \frac{\partial}{\partial x_j} T - \gamma T \frac{\partial v_j}{\partial x_j} + \frac{1}{\rho c_v}\left[\tau_{ik} \frac{\partial v_i}{\partial x_k} + \frac{\partial}{\partial x_j}\left(k \frac{\partial}{\partial x_j} T\right) + \mathcal{Q}\right] \tag{32}$$

or

$$\frac{\partial T}{\partial t} = -\frac{\partial (T v_j)}{\partial x_j} - (\gamma - 1) T \frac{\partial v_j}{\partial x_j} + \frac{1}{\rho c_v}\left[\tau_{ik} \frac{\partial v_i}{\partial x_k} + \frac{\partial}{\partial x_j}\left(k \frac{\partial}{\partial x_j} T\right) + \mathcal{Q}\right] \tag{33}$$

Thus we have an alternative expression for the *energy conservation*. Although c_v appears in Eq. (33), the latter is equivalent to Eq. (21) where c_p is used. The deviatoric stress tensor can be expressed by

$$\tau_{ik} = \eta\left(\frac{\partial v_i}{\partial x_k} + \frac{\partial v_k}{\partial x_i} - \frac{2}{3}\frac{\partial v_j}{\partial x_j}\delta_{ik}\right) \tag{34}$$

in the Eqs. (8) and (33), where η is the viscosity. For the *equation of state* we choose

$$\rho = \rho_r\left[1 - \alpha(T - T_r) + K_T^{-1}(P - P_r) + \sum_{k=1}^{2} \Gamma_k \Delta\rho_k / \rho_r\right] \tag{35}$$

where the index r refers to the adiabatic reference state, $\Delta\rho_k/\rho_r$ or f_{ak} (see Table 1) denotes the non-dimensional density jump for the kth phase transition. Γ_k is a measure of the relative fraction of the heavier phase where $\Gamma_k = \frac{1}{2}\left(1 + \tanh\frac{\pi_k}{d_k}\right)$ with $\pi_k = P - P_{0k} - \gamma_k T$ describing the excess pressure π_k. The quantity P_{0k} is the transition pressure for vanishing temperature T. A non-dimensional transition width is denoted by d_k (see Table 1). γ_k (see Table 1) represents the Clapeyron slope for the kth phase transition. Γ_k and π_k have been introduced by Richter (1973) and Christensen and Yuen (1985). Because of the very high Prandtl number, the left-hand side of Eq. (8) vanishes. So, we have the following version of the equation of *conservation of momentum*:

$$0 = -\frac{\partial}{\partial x_i}(P - P_r) + (\rho - \rho_r) g_i(r) + \frac{\partial}{\partial x_k}\tau_{ik} \tag{36}$$

The final version of the equation of *conservation of mass* is

$$0 = \frac{\partial}{\partial x_j}\rho v_j \tag{37}$$

which stems from Eq. (7). The Equations (33), (35), (36) and (37) are a system of six scalar equations we use to determine six scalar unknown functions, namely T, ρ, P and the three components of v_i.

3.3 The calculation of the functions P, ρ, K, γ, α, c_p and c_v as a function of radius

In this paper we assume *compressible* convection in a spherical shell. For our starting model with $r_n = 0$, we choose our parameters to approach earth-like conditions so far as limits on spatial resolutions allow. The viscosity, η, is the most important material parameter. It depends not only on the pressure, P, and therefore on the radius, r, but also on the temperature, T. Therefore, the viscosity has lateral and temporal dependence (see Section 3.1). As Zhang and Yuen (1996), our model includes some other quantities that weakly depend on radius. The first panel of Fig. 2 displays pressure as a

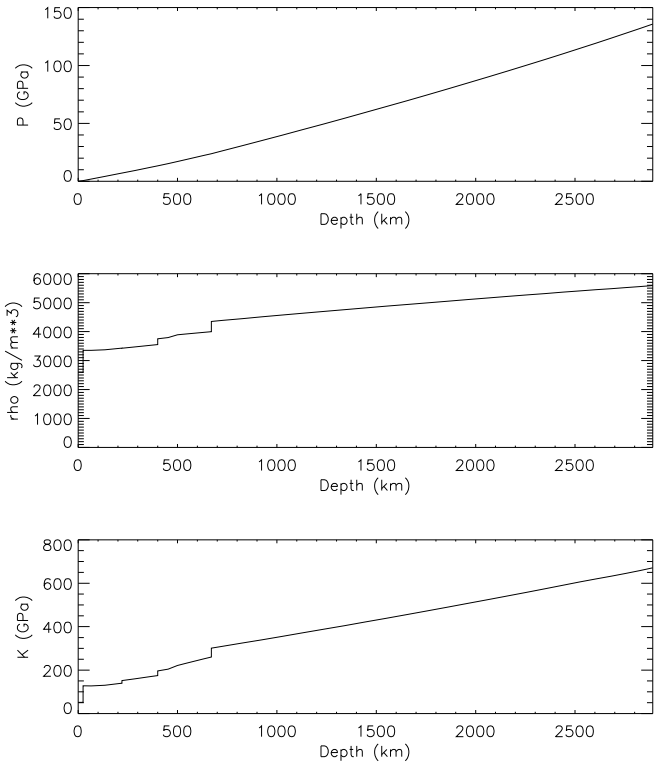

Fig. 2. The pressure, P, the density, ρ, and the bulk modulus, K, as a function of depth.

function of depth. The corresponding numerical values are taken from Table II of PREM (Dziewonski and Anderson, 1981). Our profiles for density, ρ, and bulk modulus, K, we obtain by a Birch-Murnaghan EoS, to smooth the discrete PREM fields, separately for each depth interval. Because there are only a few numerical values for ρ and K in the upper shells of the mantle, we

used a second-order Birch-Murnaghan EoS for the four shells between 0, 24.5, 220, 400, and 500 km depth. However, for the rest of the mantle we apply a third-order Birch-Murnaghan EoS. The resulting density profile is shown in the second panel of Fig. 2, while the bulk modulus profile is depicted in the third panel. The relative density jumps, f_{a1} and f_{a2}, for the major phase transitions at the top and bottom of the transition zone are given in Table 1. We use these in the calculation to make the model consistent. Irvine and Stacey (1975) calculated the free-volume Grüneisen parameter from coupled three-dimensional vibrations in a fcc crystal. We used their result

$$\gamma = \frac{\frac{1}{2} \cdot \frac{dK}{dP} - \frac{5}{6} + \frac{2}{9} \cdot \frac{P}{K}}{1 - \frac{4}{3} \cdot \frac{P}{K}} \tag{38}$$

to evaluate γ from the seismically determined but smoothed P and K. In this connection, we assume Eq. (38) may be applied to other closely packed lattices. The first panel of Fig.3 shows the Grüneisen parameter computed in this way as a function of depth. This procedure has the advantage that it involves no assumptions concerning the mantle's chemical composition. Of course, it is possible to use the more exact formula by Barton and Stacey (1985)

$$\gamma = \left[\frac{1}{2} \cdot \frac{dK}{dP} - \frac{1}{6} - \frac{1}{3} f \left(1 - \frac{1}{3} \cdot \frac{P}{K}\right)\right] \Big/ \left[1 - \frac{2}{3} f \frac{P}{K}\right] \tag{39}$$

in place of Eq. (38). In this case, for perovskite the value f is 2.27 (Stacey, 1996), assuming 6 % of the Mg atoms in $MgSiO_3$ are replaced by Fe. Using Eq. (39), however, would force us to add assumptions concerning the mineralogical composition of the mantle and to estimate $f(r)$ for the corresponding mixtures of minerals. We can show this procedure alters our model only in minor ways. We prefer to keep our model independent of the chemical composition and therefore choose $f = 2.0$ corresponding to Eq. (38).

There is no generally accepted model for the coefficient of thermal expansion, α, for the Earth's mantle. It is clear, however, that for all relevant minerals α decreases with increasing pressure. Chopelas and Boehler (1992) showed that the expansion coefficient for MgO is $5 \times 10^{-5} K^{-1}$ at adiabatically decompressed mantle conditions *(1 atm, 1700 K)*. But at the CMB pressure, α for MgO decreases to $1 \times 10^{-5} K^{-1}$. Tackley (1997) estimated $\alpha = 3.3 \times 10^{-5} K^{-1}$ at the surface and $\alpha = 1.1 \times 10^{-5} K^{-1}$ at the CMB. Stacey (1998) investigated the thermoelasticity of mineral composites for the mantle and found $\alpha = 3.35 \times 10^{-5} K^{-1}$ for the adiabatically decompressed state and $\alpha = 1.07 \times 10^{-5} K^{-1}$ at a depth of 2741 km. We choose a profile for α that varies from $\alpha = 3.46 \times 10^{-5} K^{-1}$ at the surface to $\alpha = 1.15 \times 10^{-5} K^{-1}$ at the CMB. The curvature of the profile was obtained from the formula of van den Berg and Yuen (1998, p. 223). The second panel of Fig. 3 displays the coefficient of thermal expansion of our model as a function of depth. Obviously, this is a simplification. In reality jumps in α should be expected at the upper and lower boundaries of the transition layer that are comparable to

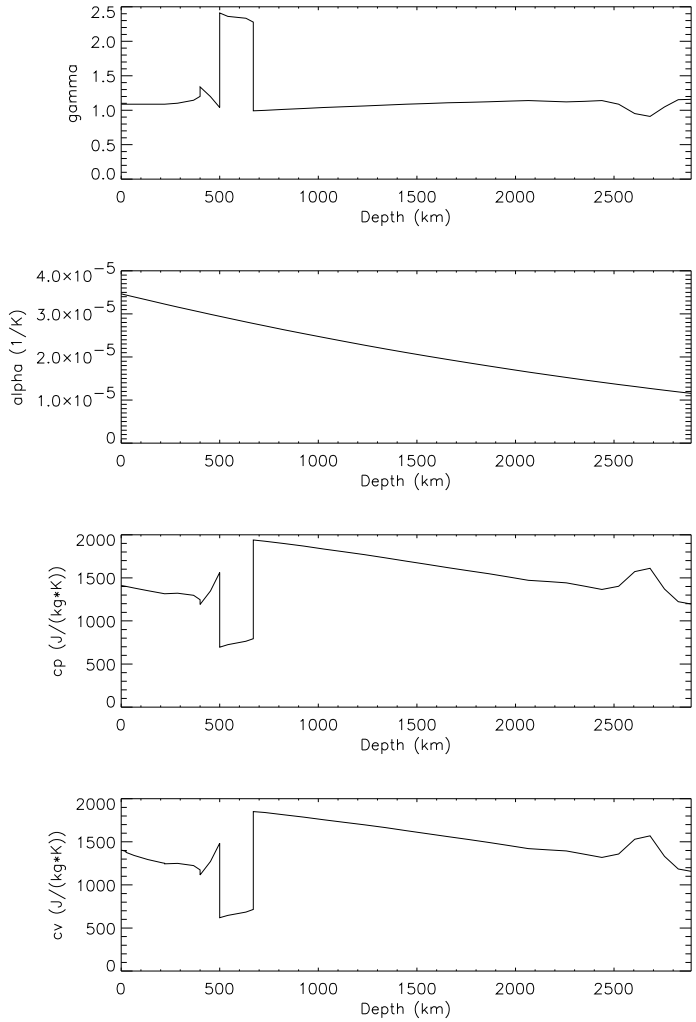

Fig. 3. The Grüneisen parameter, γ, the coefficient of thermal expansion, α, the specific heat at constant pressure, c_p, and the specific heat at constant volume, c_v, as a function of depth.

the corresponding jumps in the Grüneisen parameter. From expressions (13) and (29), we obtain the specific heat at constant pressure, c_p, and the specific heat at constant volume, c_v, as a function of depth. These are plotted in the third panel and fourth panel of Fig. 3, respectively.

3.4 Heating, initial and boundary conditions

Here, we describe some additional assumptions of the present model, S1. The age of the most meteorites is between 4.56 and 4.54 Ga (Dalrymple, 1991). It is assumed that the radioactive decay of the most important heat-producing elements began 4.56 Ga ago. If 0.07 Ga are needed for the segregation into metallic core and silicate mantle then the primordial silicate mantle was finished before $(4.49 \pm 0.03) \times 10^9$ a (McCulloch and Bennett, 1998). There is no perceivable change in the siderophile element concentrations of the rocks from the Archean to the present time (O'Neill and Palme, 1998). So, there is a high probability that the Earth's mantle and the core had no essential compositional exchange since $(4.49 \pm 0.03) \times 10^9$ a. Therefore, this age represents the beginning of the thermal mantle evolution for the present model. Walzer and Hendel (1999) computed thermal mantle convection and chemical segregation together in a 2-D model where the generation of the depleted mantle and the growth of the continental crust were obtained as a function of time. In the present paper, however, we confine ourselves to the *thermal* evolution problem alone: the silicate mantle is homogeneously heated from within and also from the CMB. It is assumed that the concentrations, $a_{\mu\nu}$, of the radioactive elements of the primordial mantle according to McCulloch and Bennett (1994) determine the internal heating (Cf. Table1). The time-dependent specific heat production, H, is computed from

$$H = \sum_{\nu=1}^{4} a_{\mu\nu} a_{if\nu} H_{0\nu} \exp(-t/\tau_\nu) \tag{40}$$

where τ_ν denotes the decay time or the $1/e$ life, $H_{0\nu}$ the initial heat generation rate per unit volume of the νth radionuclide, $a_{if\nu}$ the isotopic abundance factor, ν the indices of the four major heat-producing elements. The numerical values we use are listed in Table 2.

Table 1. Model parameters

Parameter	Description	Value	
r_{min}	Inner radius of spherical shell	3.480×10^6	m
r_{max}	Outer radius of spherical shell	6.371×10^6	m
	Temperature at the outer shell boundary	288	K
γ_1	Clapeyron slope for the olivine-spinel transition	$+3 \times 10^6$	$\mathrm{Pa{\cdot}K^{-1}}$
γ_2	Clapeyron slope for the spinel-perovskite transition	-4×10^6	$\mathrm{Pa{\cdot}K^{-1}}$
f_{a1}	Non-dimensional density jump for the olivine-spinel transition	0.0547	
f_{a2}	Non-dimensional density jump for the spinel-perovskite transition	0.0848	
	Begin of the thermal evolution of the Earth's silicate mantle	4.490×10^9	a
d_1	Non-dimensional transition width for the olivine-spinel transition	0.05	
d_2	Non-dimensional transition width for the spinel-perovskite transition	0.05	
	Begin of the radioactive decay	4.565×10^9	a
c_t	Factor of the lateral viscosity variation	2	
k	Thermal conductivity	12	$\mathrm{W{\cdot}m^{-1}{\cdot}K{-}1}$
q_{CMB}	Heat flow at the core-mantle boundary	28.9	$\mathrm{mW{\cdot}m^{-2}}$
$nr+1$	Number of radial levels	33	
	Number of grid points	1.351746×10^6	
$a_{\mu\nu}(U)$	Concentration of uranium	0.0203	ppm
$a_{\mu\nu}(Th)$	Concentration of thorium	0.0853	ppm
$a_{\mu\nu}(K)$	Concentration of potassium	250	ppm

Table 2. Data on major heat-producing isotopes

Isotope	^{40}K	^{232}K	^{235}U	^{238}U
ν	1	2	3	4
τ_ν[Ma]	2015.3	20212.2	1015.4	6446.2
$H_{0\nu}[\mathrm{Wkg^{-1}}]$	0.272×10^{-3}	0.0330×10^{-3}	47.89×10^{-3}	0.1905×10^{-3}
$a_{if\nu}$	0.000119	1	0.0071	0.9928

The heat production rate per unit volume, $\mathcal{Q}$, introduced in Section 3.2, is given by

$$\mathcal{Q} = H \cdot \rho \tag{41}$$

We assume free-slip and impermeable boundary conditions for both the Earth's surface and the CMB. What about the thermal boundary conditions? The solar luminocity has increased by some 25 % since 4.56 Ga. On the other hand, there are fluviatile and organic sediments in the Archean. Evidence of that kind shows that the average surface temperature was constant with respect to time. Obviously, some kind of thermostatic mechanism is working at

the Earth's surface, possibly the outer carbon cycle. In the contrary case, the surface temperature ought to rise, since the average distance between sun and Earth is constant because of the conservation of moment of momentum. Investigations of Archean komatiites (Sleep, 1979) and theoretical estimates of the Earth's secular cooling rate (see Schubert et al., 2001) demonstrate a decrease of about 100 K Ga^{-1} for the volumetrically averaged temperature, T_a, of the mantle. Since there is evidently no thermostatic mechanism at CMB, we ought to expect that the CMB temperature is decreasing *as a function of time*. Some authors write that it is well known that the core imposes a uniform temperature at the base of the mantle. This is right for the dependence of the location vector. For short-term convection investigations, it is a good approach to fix the CMB temperature with respect to time, too. For the *evolution* as a whole, it is very improbable that the CMB temperature is a constant *with respect to time*. Instead we assume that the CMB heat flow has been constant. Our justifications are given by Stacey's (1992) Section 6.7.5 entitled Constancy of the Core-to-Mantle Heat Flux and by Appendix A of Walzer and Hendel (1999). Anderson (1998) estimated a conductive power of $(4.4 \pm 1) \times 10^{12}$W flowing out of the core. Therefore, we assume a heat flow of 28.9 mW·m^{-2} at the CMB. Consequently, the mantle in our model, S1, is mainly heated from within but also somewhat from below. For the overall mechanism of our model, this assumption is not very important. If we use Tackley's (2000b) assumption of zero heat flow at CMB the planforms in the upper half of the mantle stay very similar. Only the plumes are reduced. We could be tempted to replace the assumption of a constant core-to-mantle heat flow, q_{CMB}, by a prescribed decaying q_{CMB}. However, Stevenson et al. (1983) showed that the onset of inner core freezeout leads to slightly rising or nearly constant q_{CMB}-values of about 23 mW·m^{-2} for the second half of the Earth's history (see also Schubert et al., 2001, pp.607-609). The temporally and laterally averaged surface temperature of the Earth was 288 K for the last 40 years. We assume this value as the constant surface temperature of the model.

3.5 Numerical method and implementation

The solutions of the system of differential equations of convection in a compressional spherical shell, Eqs. (33) to (37) with the additional Eqs. (5), (40) and (41), are obtained using a three-dimensional finite-element method, a fast multigrid solver and the second-order Runge-Kutta procedure. The mesh is generated by projection of a regular icosahedron onto a sphere to devide the spherical surface into twenty spherical triangles or ten spherical diamonds. A dyadic mesh refinement procedure connects the midpoints of each side of a triangle with a great circle such that each triangle is subdivided into four smaller triangles. Successive grid refinements generate an almost uniform triangular discretization of the spherical surface of the desired resolution. Corresponding mesh points of spherical surfaces at different depths are connected by radial lines. The radial distribution of the different spherical-surface triangular net-

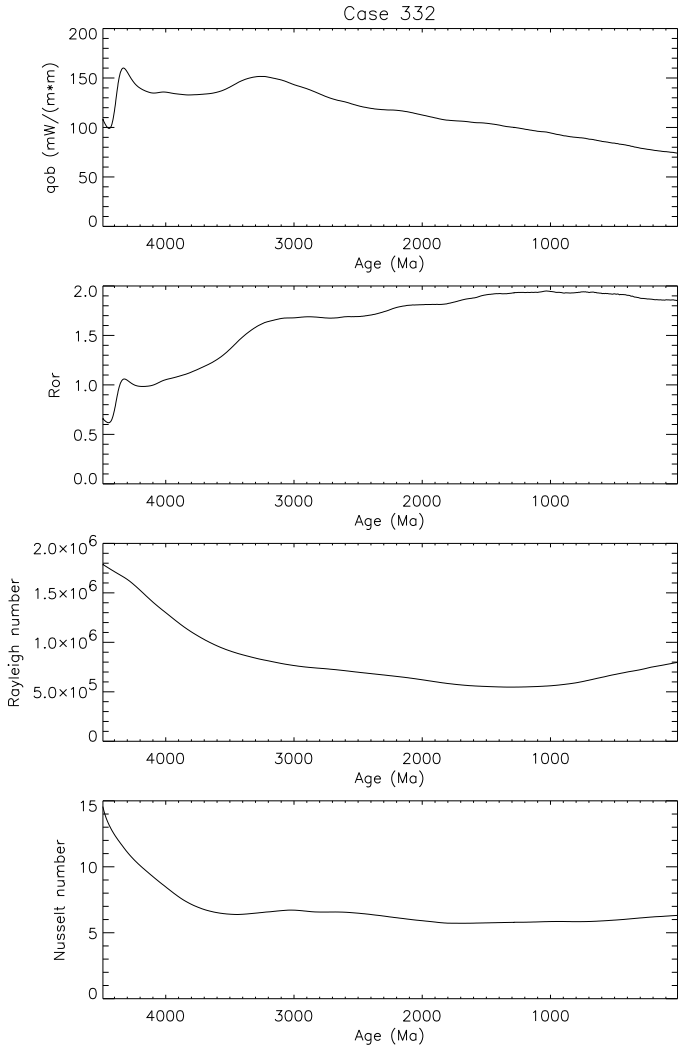

Fig. 4. The evolution of the laterally averaged surface heat flow, *qob*, of the ratio of the surface heat outflow per unit time to the mantle's radiogenic heat production per unit time, *Ror*, of the Rayleigh number, *Ra*, and of the Nusselt number, Nu.

works is so that the volumes of the cells are nearly equal. More details are given by Baumgardner (1983, 1985), Bunge et al. (1997) and Yang (1997). For the multitude of runs we needed for our parameter study, we employed a mesh with 1351746 nodes. Some runs were made with 10649730 nodes to check the convergence of the lower resolution runs. The result is that the laterally averaged heat flow, the ratio of heat outflow to radiogenic heat production, the Rayleigh number, and the Nusselt number as functions of the time show

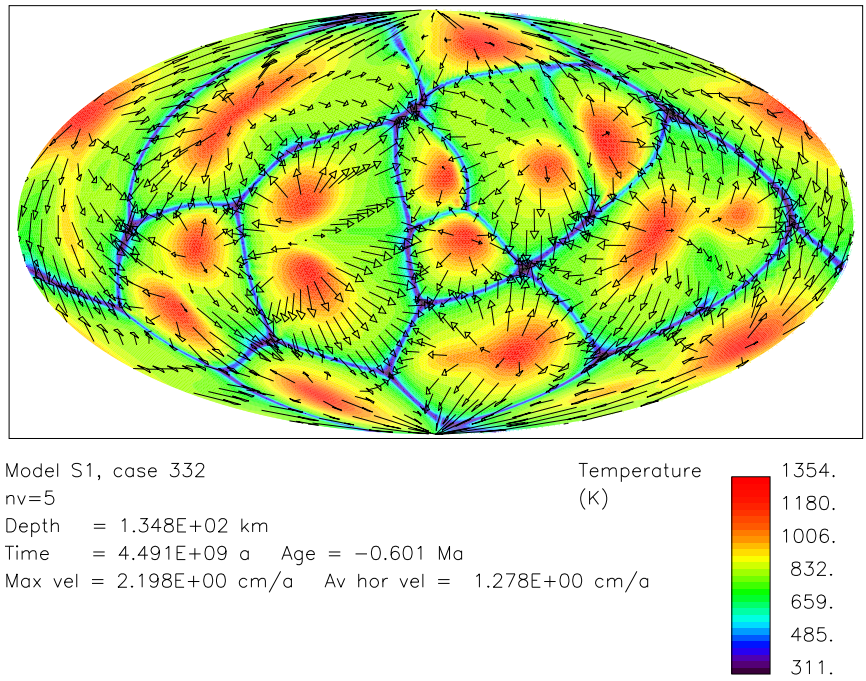

Fig. 5. (a) Spherical-shell convection of a Newtonian fluid heated from within and slightly from below with depth- and temperature-dependent viscosity. The radial factor of the viscosity is given by Fig.1. An equal-area projection of the planforms at various depths: (a) 134.8 km, (b) 632.9 km, (c) 1130 km, (d) 1551 km. Temperature is denoted by colors, creeping velocity by arrows.

hardly any discernable differences (< 0.5 %). Calculations were performed on 128 processors of a Cray T3E. A scalability test showed a scaling degree of nearly 90 %. The code uses all processor–processor communications with the same load. This is optimal for the T3E architecture. A hierarchically organized processor connection could not be effectively used by the code without a basic time wasting reconstruction. The code was benchmarked for constant viscosity convection by Bunge et al. (1997) with numerical results of Glatzmaier (1988) for Nusselt numbers, peak temperatures, and peak velocities. A good agreement (≤ 1.5 %) was found.

4 Results

4.1 Thin cold sheet-like downwellings

Before we examine results from our parameter study, we will describe the numerical results from our reference model with $r_n = 0$. We anticipate that

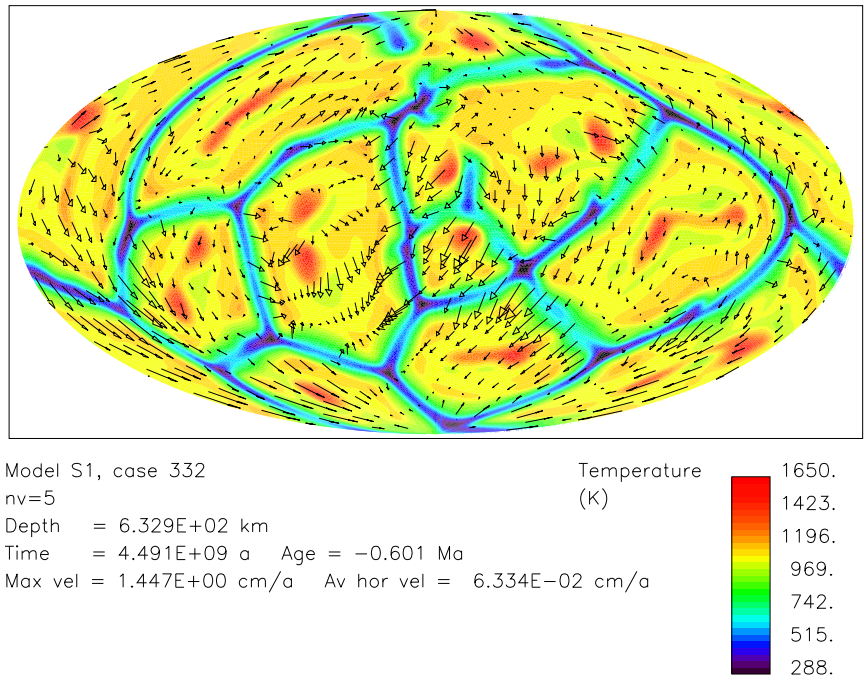

Fig. 5. (b) Text see Fig. 5. (a). Here: 632.9 km depth

the main features of the solutions, especially of the planforms that we describe here, apply also for a wider range of Rayleigh numbers. The first panel of Fig. 4 shows the averaged heat flow at the Earth's surface as a function of time in the past. The present-day heat flow from the starting model is 74.0 mW·m^{-2}. By comparison Pollack et al. (1993) found a mean global heat flow of 87 mW·m^{-2} for the present Earth based on 24774 heat flow measurements. Apart from some initial transient behavior, the heat flow of the model declines in a smooth fashion. The *r*atio of the heat *o*utflow per unit of time to the *r*adiogenic heat produced in the mantle per unit of time, *Ror*, is displayed in the second panel of Fig. 4. The present-day value of *Ror* is 1.851. Note that since about 2000 Ma the value of *Ror* changes only slightly. By way of comparison, Stacey and Stacey (1999) estimate 14.4×10^{30} J for the total heat loss of the Earth and 7.8×10^{30} J for the radiogenic heat of the Earth. The quotient of these two numbers is 1.846. *Ror* is the reciprocal value of the Urey number. The third panel of Fig. 4 shows the time history of the Rayleigh number, while the fourth panel of Fig. 4 depicts the time history of Nusselt number.
Because of Section 3.4, the Rayleigh number

$$Ra = \left\langle \frac{\rho\alpha g h^3}{\kappa\eta_{al}} \cdot \frac{(\mathcal{Q}h + q_{CMB})h}{k} \right\rangle \tag{42}$$

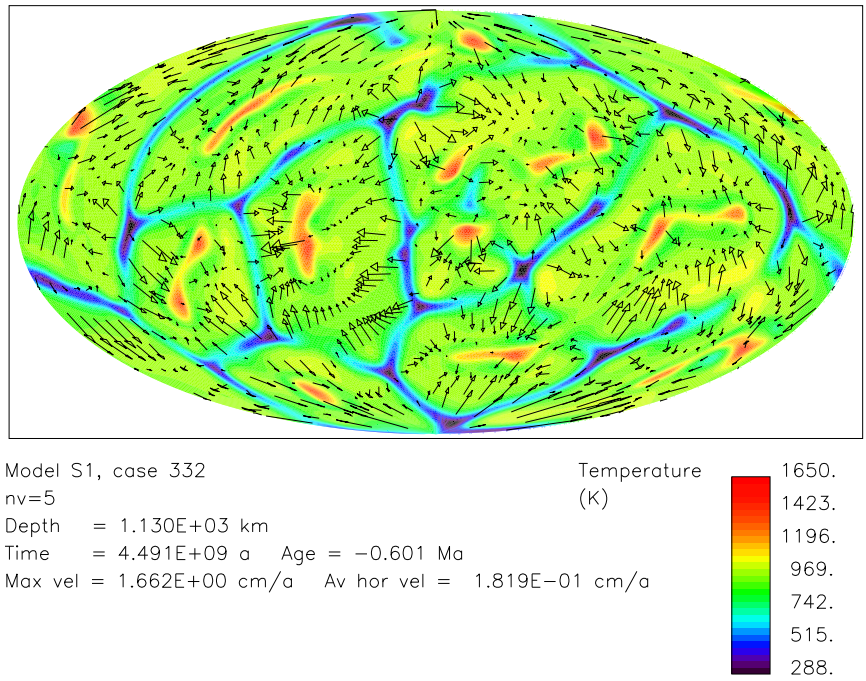

Fig. 5. (c) Text see Fig. 5. (a). Here: 1130 km depth

is better adapted to the problem than

$$Ra_B = \left\langle \frac{\rho \alpha g h^3}{\kappa \eta_{al}} \right\rangle \cdot \Delta T \tag{43}$$

since the mantle is mainly heated from within. The bracket $\langle\ \rangle$ denotes a volumetric average but not a temporal average. The temperature difference, ΔT, across the mantle is not constant for the *evolution* problem (see Section 3.4.). h is depth of CMB, κ is thermal diffusivity. $\mathcal{Q}$ is defined by Eqs. (40) and (41). Therefore, the heat generation rate per volume, $\mathcal{Q}$, is monotonously declining as a function of time. The quantity η_{al} is given by

$$\log \eta_{al} = \langle \log \eta \rangle \tag{44}$$

The quantity η_{al} is also a function of time because of Eqs. (5) and (44). Therefore Ra is a function of time. The Nusselt number, Nu, is the ratio of the actual heat flow to the purely conductive heat flow down the superadiabatic temperature gradient. Nu is a function of time, too.
Fig. 5 presents the temperature distribution (multicolored) and the solid-state creep velocities (arrows) on equal-area projections for different depths. These pictures are computed for the geological present using the radial viscosity

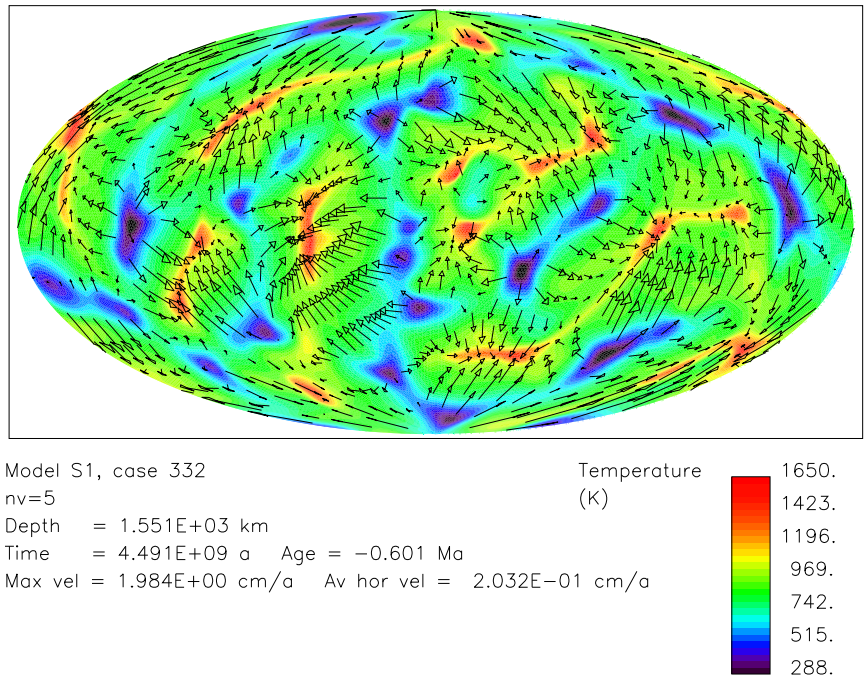

Fig. 5. (d) Text see Fig. 5. (a). Here: 1551 km depth

profile of Fig. 1. The *narrow blue stripes* of Fig. 5(a) at 135 km depth are remarkable and represent a network of interconnected downwelling sheets of cold material. Fig. 5(b) shows that these sheets maintain their identity at a depth of 633 km, and are sinking vertically with neglible horizontal displacement. This reflects the simplicity of our treatment of the cold upper boundary layer, a treatment that lacks buoyant continents, one-sided subduction, and other plate-like features. Fig. 5(c) reveals that the thin downwelling sheets persist to 1130 km depth. By 1550 km depth, however, the sheet-like character of the downwellings has largely vanished as shown in Fig. 5(d). This fact is probably a consequence of the viscosity hill of the lower mantle (Cf. Fig. 1). Figs. 4 and 5 apply for a run with $r_n = 0$. For higher values of r_n, however, the thin sheets dip deeper into the mantle. Two features of our solutions are noteworthy:

a) Other published convection models with Newtonian rheology display much wider zones of downwelling near the surface and

b) the relatively thin downwelling sheets in the present model freely penetrate the high-viscosity transition layer.

For lack of space, we do not include a temporal sequence of plots of temperature and velocity from the early Archean (4000 Ma) to the present. However,

the pattern of a network of thin downwelling sheets appears very early in the calculation and changes only slowly with time. In the first 2000 Ma, some new sheets form to subdivide originally oblong convective cells. In the last 2000 Ma, no new sheets appear, but some cells slowly grow, while other cells slowly shrink. In general the positions of the cell centers are nearly stable.

4.2 Variation of non-dimensional numbers

We vary the parameter r_n of Eq. (5) in the interval $-0.5 \leq r_n \leq +1.5$. This is a first step to become independent of the special results of the geophysically derived viscosity model. First of all we don't alter η_1, i.e., only the level of the radial reference viscosity profile is shifted as a whole without the altered temperature influence on the viscosity that is included in the further computation, too. The thickness of the subducting downwelling sheets decreases with decreasing negative values of r_n down to -0.5, i.e. for higher Rayleigh numbers. In this way, the blue lines on the equal-area projection plots become thinner and thinner with decreasing r_n. Up to $r_n = +0.3$, the cold sheet-like downwellings are rather thin yet, but the thickness slightly grows with increasing r_n. The more the quantity r_n increases, the deeper the sheet-like structures can be distinguished.
Now comes the main point: *quantification* of the results. Fig. 6 shows the dependence of the Rayleigh number, Ra, on the non-dimensional viscosity level parameter, r_n. The definition of Ra is given by Eq. (42). It is an essential feature of the evolution of the Earth that its direction is defined by irreversible processes, especially that the heat generation rate per volume, $\mathcal{Q}$, decreases with time and that the Earth cools down, i.e., that the volumetrically averaged temperature, T_a, diminishes. The latter process would happen, of course, also if the internal heating would take place only at the beginning by accretion. Therefore η_{al} rises as a function of time (Cf. Eqs. (5) and (44)). On the other hand, $\mathcal{Q}$, grows less because of the exponentially decreasing radioactive decay (Cf. Eg. (40)). So for all r_n, the Rayleigh number decreases as a function of time (Cf. Fig. 6 and capture). Initially, Ra diminishes quickly, then only slowly, nearly independent of r_n. On that account we computed the temporal average of Ra only for the last 2000 Ma and called it $Ra_{(2)}$. In a similar way, Fig. 7 represents the Nusselt number, Nu, for different ages as a function of r_n. For the interval $-0.3 \leq r_n \leq +0.1$, Nu, decreases somewhat in the beginning and fluctuates only slightly around a rather stable value for the main part of the evolution. For the same r_n-interval, the sheet-like downwellings are not only marked but they stretch deeper into the mantle than for runs with smaller r_n and higher Ra. Fig.8 displays Ror for different ages as a function of r_n. For the last 2000 Ma and $-0.1 \leq r_n \leq +0.1$, the reciprocal value, Ror, of the Urey number is rather near the 1.85 value that has been derived by Stacey and Stacey (1999). The interval $+1.2 \leq r_n \leq +1.4$ has to be excluded since the Nusselt numbers are too low in this range. For runs with $-0.5 \leq r_n \leq +0.7$, Ror does not vary about very much for the last 2000 Ma.

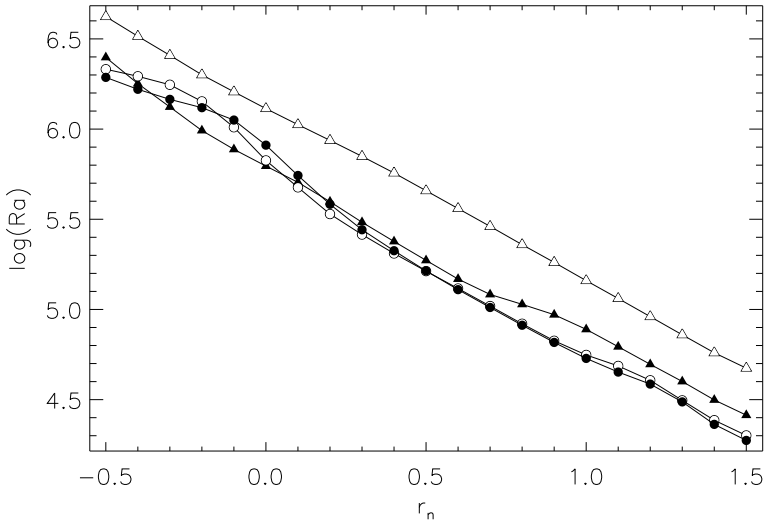

Fig. 6. The Rayleigh number, $Ra(t)$, as a function of the non-dimensional viscosity-level parameter, r_n. Open triangles represent an age of 4000 Ma, filled triangles stand for 2000 Ma, open circles for 500 Ma, filled circles for 0 Ma.

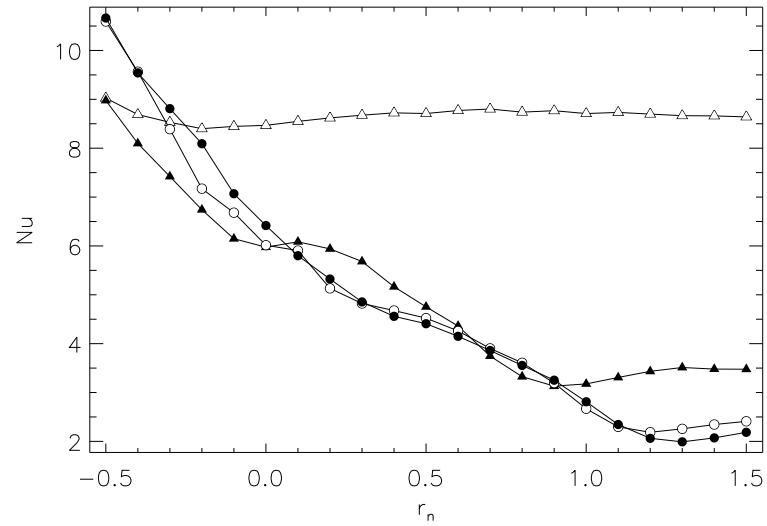

Fig. 7. The Nusselt number $Nu(t)$, vs. r_n. For explanation of symbols see Fig. 6.

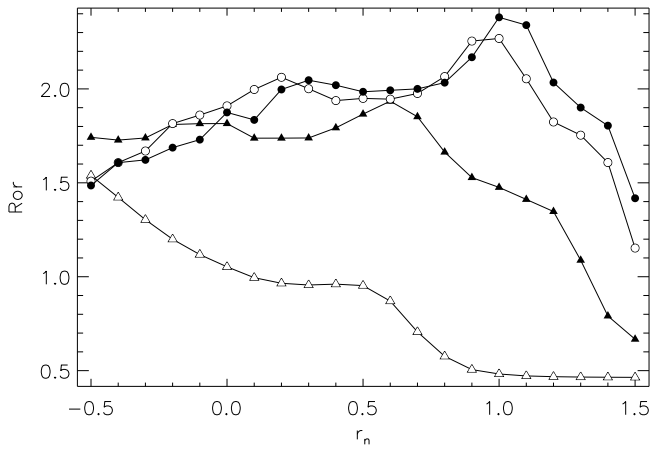

Fig. 8. The reciprocal value, $Ror(t)$, of the Urey number, versus r_n. For explanation of symbols see Fig. 6.

Although formulae like

$$Nu = cRa^{\beta} \tag{45}$$

apply only for convection with constant viscosity and since certain parameterized steady-state convection models employ Eq. (45), we carry out the following simple evaluation. Of course, Nu and Ra are functions of the time in our more complex non-steady evolution model. We obtain $Nu_{(2)}$ and $Ra_{(2)}$ calculating the temporal average of $Nu(t)$ and $Ra(t)$, respectively, for the last 2000 Ma. $Nu_{(2)}$ is plotted versus $Ra_{(2)}$ in Fig. 9. Each black square represents one run. The solid curve is a least square fit to a power law similar to Eq. (45). We obtained

$$Nu_{(2)} = 0.120 Ra_{(2)}^{0.295} \tag{46}$$

In Section 5 we discuss why Eq.(46) describes the $Nu_{(2)}$ – $Ra_{(2)}$ relation of the numerical experiments in a rough approximation and why Eq. (46) is similar to the Nu – Ra relation of simple steady-state convection models with constant viscosity. A further set of runs showed that the radial profiles of γ, α, c_ν and c_p (Cf. Fig. 3) have only minor influence: Planforms as well as the non-dimensional numbers Ra, Nu and Ror alter only slightly. Therefore and for lack of space the corresponding plots are not presented here. Furthermore, we introduced a volumetrically averaged Grüneisen parameter, γ_b, instead of the radial gamma profile (Cf. Fig.3, first panel). Subsequently, this γ_b-value has been varied. The results of the runs, e.g. the non-dimensional numbers and temperature-plus-velocity plots, proved to be rather robust. As an example, Fig. 10 shows Nu as a function of γ_b and reveals that the temporal dependence of Nu is much stronger than the γ_b-dependence. Fig. 11 displays $Ror_{(2)}$ versus r_n where $Ror_{(2)}$ is the temporal average of Ror for the last 2000 Ma. The

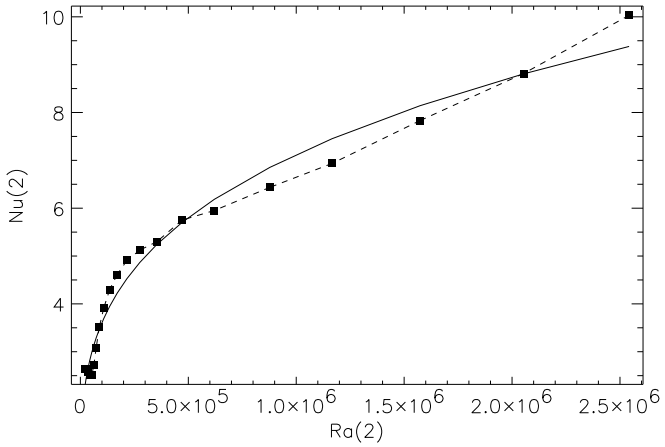

Fig. 9. An average Nusselt number, $Nu_{(2)}$, versus an average Rayleigh number, $Ra_{(2)}$. The supplement (2) stands for the time average of the proper quantity over the last 2000 Ma. Filled squares represent the results of different runs. The solid curve is a non-linear least square fit to a power law of the form $Nu_{(2)} = c\ Ra^{\beta}_{(2)}$ where $c = 0.120$ and $\beta = 0.295$.

value $Ror = 1.85$ according to Stacey and Stacey (1999) can be found at about $r_n = -0.1$ and $r_n = +1.1$. Figs. 6 and 7 show that $r_n = +1.1$ must drop out since otherwise Ra and Nu would be extremely low.

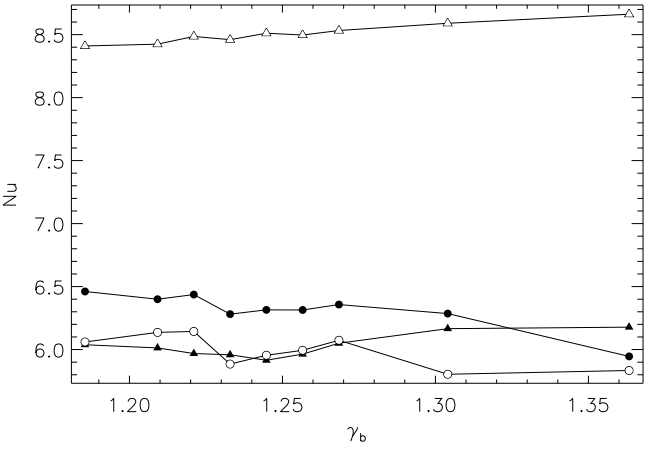

Fig. 10. The Nusselt number, $Nu(t)$, as a function of the volumetrically averaged Grüneisen parameter, γ_b. For explanation of symbols see Fig. 6.

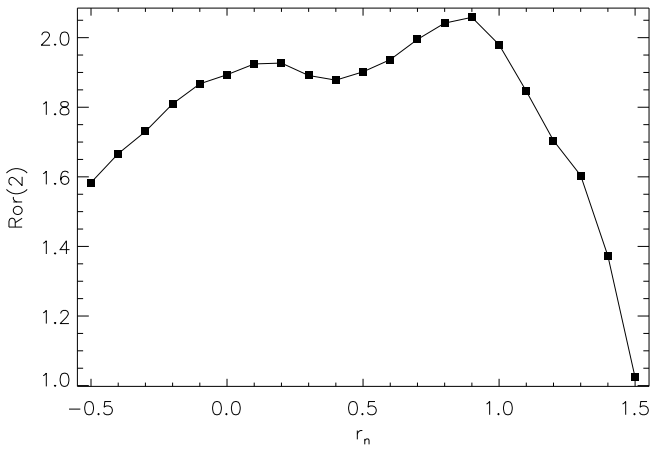

Fig. 11. The reciprocal value, $Ror_{(2)}$, of the average Urey number versus r_n. The supplement (2) denotes the time average of *Ror* over the last 2000 Ma.

4.3 Effects of r_n-variations on planforms. Further variation of model parameters

If, because of the last remarks, $r_n = -0.1$ is regarded as the optimum value of r_n then we should have a look at the other results of the relevant run. The first panel of Fig. 12 shows a laterally averaged surface heat flow that decreases during nearly the whole Earth's history and has a present value of 69.1 mWm^{-2}. The variations of *Ror* during the last 2000 Ma are small. The present value is 1.73. The curve of the Rayleigh number arrives at 1.12×10^6 for today, and the present-day Nusselt number is 7.07. The last panel of Fig. 12 reveals that Nu is nearly a constant since about 4000 Ma. Fig. 13 represents the present-day distribution of temperature and creeping velocity in 134.8 km depth for $r_n = -0.1$. As expected, there is no plate-like velocity distribution near the surface since it is a Newtonian-fluid model. However, the thickness of the blue lines is smaller yet than in the case with $r_n = 0.0$ (Cf. Fig. 5(a)). The network of the sheet-like downwellings of both pictures is related but in Fig. 13 some sheets are missing. The network of plate-like subducting zones shows distinct outlines in 1150 km depth, yet. In greater depths, the tendency to oblong isothermal lines gradually vanishes.

A few runs were performed with equivalent parameters but with an incompressible EoS. The structure of the planforms was similar but the downwellings were broader.

We also examined the effect of switching off the lateral temperature dependence of the viscosity. The results confirm the prevailing wisdom that the

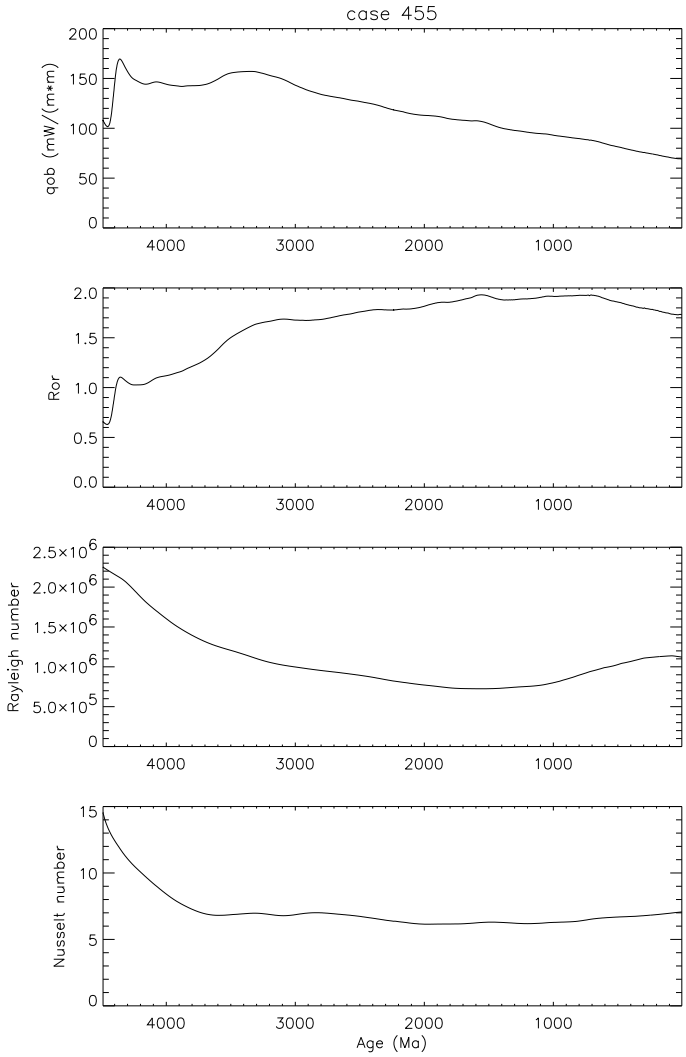

Fig. 12. For $r_n = -0.1$, the time dependence curves of the following quantities are shown: laterally averaged surface heat flow, *qob*, the reciprocal value, *Ror*, of the Urey number, the Rayleigh number, *Ra*, and the Nusselt number, Nu.

radial viscosity variation (Cf. Fig.1) is the decisive variation. We did not vary the heating since the various chemical models for the Earth show only minor differences regarding the concentration of the heat-producing elements in the primordial mantle.

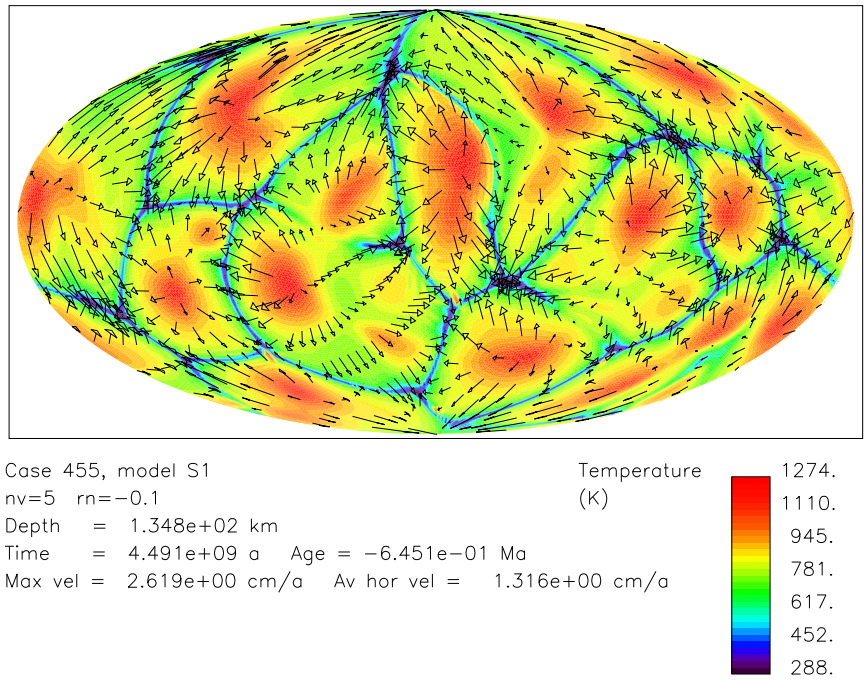

Fig. 13. For $r_n = -0.1$, temperature (color) and the creeping velocity (arrows) are depicted on an equal-area projection of a spherical surface in 134.8 km depth for the present time.

4.4 Runs with radial viscosity profiles without a second low-viscosity layer

After confirming that variation in the viscosity level had the largest influence on the results we sought to explore the effects of altering the profile. Although the radial profile of Fig.1 seemed realistic on the basis of solid-state physics and seismology, we decreased the viscosity minimum at the top of the lower mantle stepwise until it vanished, to check its influence on the fluid mechanics. Fig. 14 is the extreme case of such a profile. We ran a case with this viscosity profile but everything else identical to our reference model. Fig. 15 reveals the evolution of the laterally averaged surface heat flow, *qob*, the reciprocal value, *Ror*, of the Urey number, the Rayleigh number, Ra, and the Nusselt number, Nu. Fig. 16 is the counterpart of the Fig. 5(a). Fig. 16 shows broader downwelling sheets than Fig.5(a). The number of cells is reduced. For the depths 632.9 and 1130 km, the downwelling zones are considerably less slab-like. The dissolution of these structures at 1550 km depth was very pronounced in Fig. 5(d), but is less so in the counterpart plot without second low-viscosity layer beneath the transition zone. The explanation seems to be that long

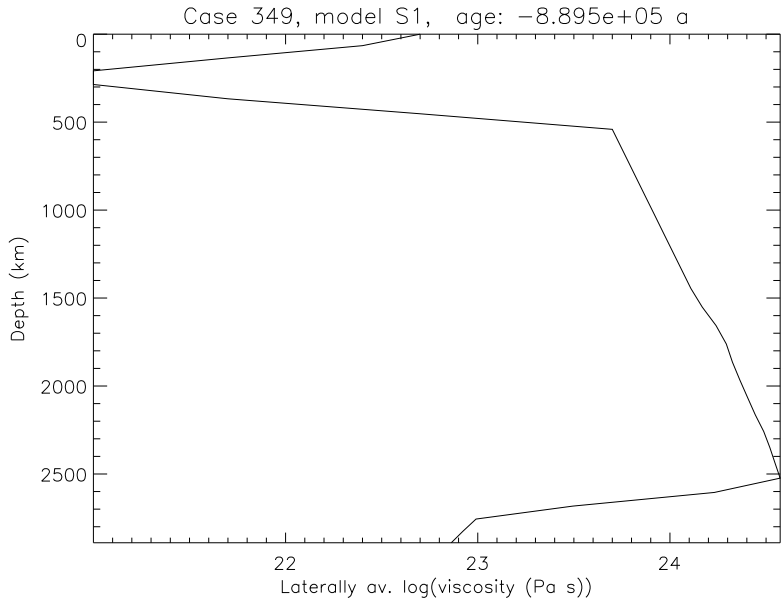

Fig. 14. An alternative basic radial viscosity profile, $\eta_2(r)$, for $r_n = 0$.

wavelength downwelling structures can penetrate deeper into the viscosity hill of the lower mantle than short wavelength ones.

5 Discussion and conclusions

We begin with some remarks on our starting radial viscosity profile. In spite of the runs we performed in connection with Sections 4.2., 4.3. and 4.4., it is our opinion that a viscosity profile with two minima in the upper half of the mantle is realistic based on solid-state physics and PREM (Cf. Fig.1). We shall review briefly some relevant papers that provide hints in this direction but have been obtained using other methods. Spada et al. (1992) investigated effects on post-glacial rebound from a high-viscosity transition layer. They found that a hard layer between 410 and 660 km depth diminishes ones ability to fit polar wander data with a small viscosity increase across the lower mantle. Therefore, a prominent maximum in viscosity in the lower mantle (Cf. Fig.1) appears necessary not only because the melting temperature increases with increasing pressure (and thereby represents an estimate of the activation enthalpy) but also for purely geophysical reasons. The seismic activity along the passive margins of Fennoscandia requires a remarkable viscosity increase below the asthenosphere, most likely in the transition layer. Čížková et al. (1996) and Kido and Čadek (1997) also argued for the existence of a high viscosity transition layer and of two low viscosity layers, one above and one

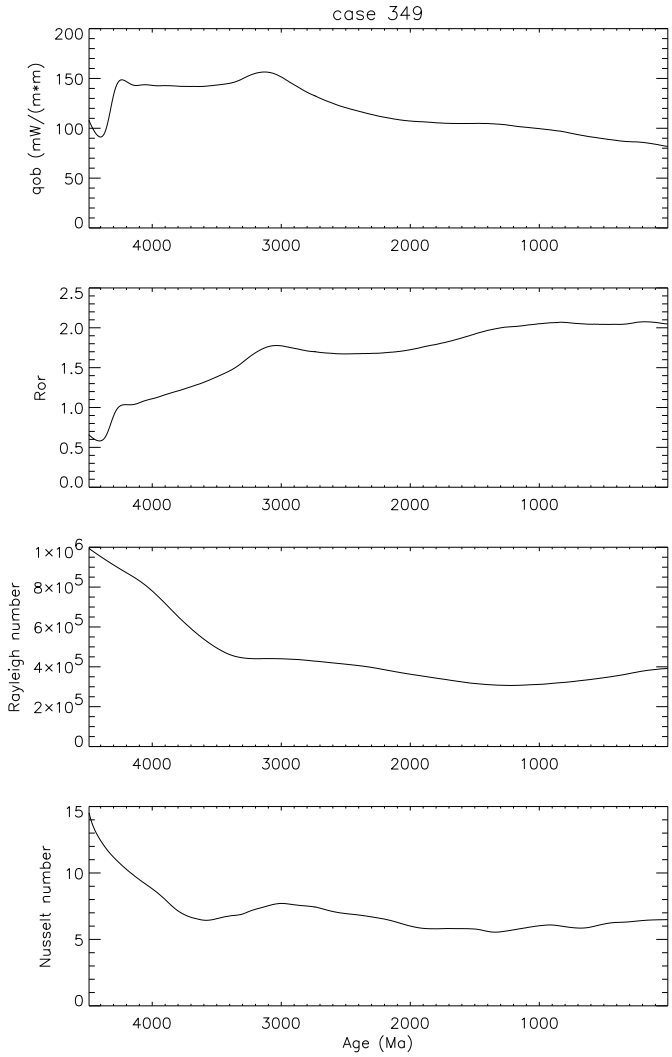

Fig. 15. For $\eta_2(r)$, the time dependence of the following quantities is shown: laterally averaged surface heat flow, *qob*, the reciprocal value, *Ror*, of the Urey number, the Rayleigh number, *Ra*, and the Nusselt number, Nu.

below of it. They started from a distribution of the seismic velocities by Li and Romanowicz (1996), transformed the seismic velocities into densities, and used a genetic algorithmic inversion that excluded those parts of the mantle where the density differences have predominantly compositional causes. Using intermediate-wavelength geoid inversions, Kido and Yuen (2000) studied the viscosity profile of the mid-mantle in detail. They found it to be of no major consequence whether they introduced an impermeable boundary at

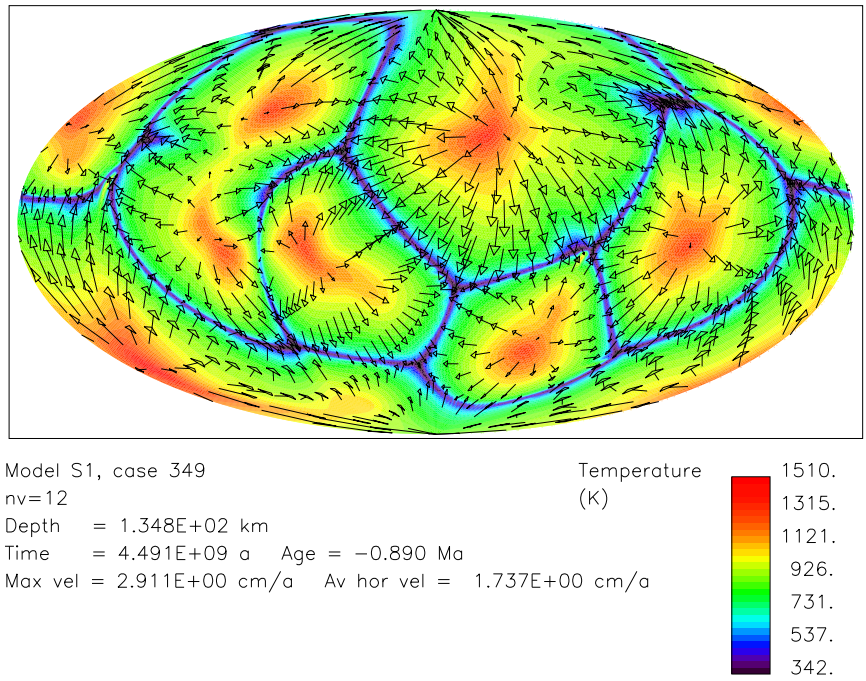

Fig. 16. For $\eta_2(r)$, temperature (color) and the creeping velocity (arrows) is displayed on an equal-area projection of a spherical surface in 134.8 km depth for the present time.

660, 700, 750, or even 1000 km depth or whether there was no impermeable boundary. In all cases they obtained similar viscosity profiles, namely, a high viscosity lithosphere, followed by a low viscosity asthenosphere, followed by a high-viscosity transition layer, followed by a second low viscosity layer in the uppermost part of the lower mantle. Their curves are similar to the upper half of Fig.1. They did not show the profile for the lower half of the mantle because of low resolution. Forte (2000) derived a set of viscosity profiles through a formal inversion procedure. His profiles produce a best fit to the observed free-air anomalies and to the observed motions of the lithospheric plates where his starting point was a pair of seismic tomography models. When an impermeable boundary is assumed at 670 km depth, the resulting viscosity-depth curve is similar to our Fig.1. Whithout this impermeable boundary the viscosity peak, corresponding to the transition layer, is shifted down by 240 km. As a final remark on the starting profile, the observed peak in deep-focus seismicity at transition zone depths (Kirby et al., 1996), and the non-occurence of earthquakes deeper than 700 km, despite tomographic evidence for slab penetration into the lower mantle, supports our inference of

a high-viscosity transition layer with low-viscosity layer immediately below it. However, in the course of the work we gained a certain independence of the starting viscosity profile by variation of the parameters.

The present paper describes a set of numerical experiments with an infinite Prandtl number fluid in a compressible spherical shell heated mainly from within. We used the anelastic liquid approximation with Earth-like material parameters. The Birch-Murnaghan EoS was employed to derive the Grüneisen parameter, isothermal bulk modulus and its pressure derivative as a function of depth from observational values provided by PREM. We computed the melting temperature as a function of depth using the Grüneisen parameter, Lindemann's law and some solid-state physics considerations. Since the melting temperature can be regarded as a proxy for activation enthalpy, we use it to estimate the radial viscosity variation. We calibrated this relative profile by the value of the asthenospheric viscosity that matches post-glacial rebound observations. In addition, we include the lateral dependence of viscosity on temperature such that the viscosity depends on the radius, the colatitude, the longitude, and the time.

A lot of other models reduce the variability of the viscosity to the temperature dependence. In the corresponding convection models, the boundary layers at the upper surface and at the CMB control the mechanism (Cf. Section 2.) and the bulk of the mantle is isoviscous. Since none of the three possible convection regimes shows plate-like velocities near the surface, some groups introduced other constitutive equations that differ from the Newtonian fluid. New rheologies have been used in order to reproduce lithospheric strain localization and weakening. E.g., Tackley (2000a) investigated the influence of viscoplastic yield stress where a part of it depended on depth. Tackley (2000b) studied the effect of increasing strain weakening. Richards et al. (2001) found that the generation of plates is facilitated by plastic yield stress and a low-viscosity asthenosphere beneath the lithosphere. Bercovici et al. (2001b,c,2002) and Ricard et al. (2001) examined a two-phase mixture to achieve a continuum description of weakening and shear localization and to explain the plate boundary formation. Continuing the work of Trompert and Hansen (1998), the Hansen group is working on the problem of the formation of oceanic lithosphere and subduction slabs, too. It is fully legitimate that this main problem attracts so much attention and efforts.

However, the focus of the present paper is the influence of the physical material properties, especially of the viscosity, *inside* the mantle on the thermal *evolution*, hence preferably on the development of convection during a long time interval. Karato (1997a) concluded that in the typical mantle, where temperature is moderately high and stress is relatively low, the dominant creeping mechanism is either diffusion creep or power law. We suppose that a Newtonian fluid is an acceptable approximation for the main part of the mantle since the prevailing gradients of the creeping velocity are probably sufficiently small in the lower mantle and in the transition zone. First we report briefly on the less important point: We found by variation of

the parameters that the influence of γ, α, c_ν and c_p is small compared with the viscosity effect. This statement applies for constant values of γ, α, c_ν and c_p as well as for the radial profiles of these quantities that have been derived from physics and geophysics.
It is however most important that, for the reasons a) and b) of Section 2., the viscosity profile is stronger dependent on the radius than often assumed. Our preferred viscosity profile displays not only a high-viscosity lithosphere and a viscosity hill in the lower portion of the lower mantle but, also a prominent *high-viscosity transition layer* inferred to arise from a high garnet content. Moreover, there is not only the usual asthenosphere but also a *second low-viscosity zone just below the 660-km* phase boundary. We note that our preferred viscosity profile bears a similarity to the successful viscosity profile LVZ of Cserepes et al. (2000, p. 139) and to the profile VL of Forte (2000) that is based on mantle flow calculations in which the density contrasts were estimated from long-wavelength seismic heterogeneity assuming density differences are caused exclusively by temperature differences. The computed flows were constrained to match observed free-air gravity anomalies and observed tectonic plate motions.
Systematic variation of the viscosity-level parameter, r_n, shows the following result within wide boundaries ($-0.5 \leq r_n \leq +0.3$): *The existence of two low-viscosity layers inside the mantle causes networks of very thin tabular-shaped downwellings*. These sheets are considerably thinner than other downwellings of known Newtonian-fluid models. The quantity r_n can be transformed into the Rayleigh number using Fig.6 or, more exactly, Eq. (5). *The plate-like downwelling sheets are thin down to about 1350 km depth.* Hence, they are able to penetrate the high-viscosity transition layer. The sheets begin to assume the form of large drop shaped features at a depth of about 1550 km. Of course, our solutions have no plates at the surface. A natural way to get plates would probably be to take into account the different oceanic-lithospheric layers with different constitutive equations, from top to bottom brittle, semi-brittle and viscoplastic (Kohlstedt et al., 1995). But the incorporation of this stratification in a flow model is a problem of node distance. Furthermore, the incorporation of water in the oceanic crust seems to be an important cause for the possibility of subduction: Terrestrial planets without oceans don't have plate tectonics. Another important effect is the dehydration of the harzburgite that occurs during partial melting. This is likely to increase the slab viscosity by 2-3 orders of magnitude (Braun et al., 2000). All these effects are not included in our model.

We found extremely well developed thin sheet-like downwellings are in the surrounding of $r_n = -0.1$. This corresponds to the *Ror* value by Stacey and Stacey (1999). For the interval $-0.5 \leq r_n \leq +0.7$, *Ror* varies only slightly as a function of time during the last 2000 Ma. An interesting result is the *nearly time-independent Nusselt number for* $-0.3 \leq r_n \leq +0.1$ *and the last 4000 Ma*

of evolution. All the mentioned major trends in our results are robust at least for $-0.3 \leq r_n \leq +0.1$.
The transformation of the sheet-like downwellings into broader drop-like structures can be demonstrated by a comparison between Figs. 5 (c) and 5 (d). The depth of this transformation increases with growing r_n. The mentioned transformation can be observed also in the real mantle: Seismic tomographic models change their statistical character between 1400 and 1900 km depth. P-wave and S-wave velocity deviations are decorrelated in the deep mantle (van der Hilst and Kárason, 1999; Davaille, 1999). Most subducting slabs do not extend deeper than 1700 km (van der Hilst et al., 1997). *This is well compatible with a high-viscosity lower part of the lower mantle.*
The more the Rayleigh number has been augmented and the nearer the approach is therefore to Earth-like Rayleigh numbers the more sheet-like are the downwellings of our model. For reasons of solid-state physics, we think that steeper viscosity gradients near 410, 520 and 660 km depth are unavoidable for the real Earth. For numerical reasons, however, we have been forced to diminish these viscosity gradients. Our numerical experiments show: The steeper these gradients are the less vertical mass flow can be observed at the corresponding depth. Therefore we anticipate that the real transition layer is a kind of barriere for mantle convection but a permeable one. However, for the *present* viscosity profile we obtained whole-mantle convection that is sluggish in the lower part of the lower mantle. The large radial variations of the viscosity proved to be very important for the horizontal length scales of the flow patterns. They were more relevant than the temperature dependence of the viscosity. The latter result corresponds with that of Ratcliff et al. (1997).
Howard (1966), Parsons and McKenzie (1978) and Kenyon and Turcotte (1983) performed a simple boundary stability analysis for an incompressible viscous fluid in a horizontal layer with constant material parameters, with prescribed boundary temperatures, without internal heating and free-slip boundary conditions. The heat loss at the surface is conductive. Non-zero thermal gradients exist only in the boundary layers. The boundary layers will gradually thicken and break away if enough buoyancy is collected. For this problem

$$Nu = 0.112 Ra^{0.333} \tag{47}$$

has been deduced. It is surprising that our non-steady compressible-shell evolution model with depth- and temperature-dependent viscosity and mainly internal, temporally decreasing heating has led to the result that the numerical experiments can be summarized by Eq. (46) and Fig.9. Stagnant-lid convection regimes established other Nu– Ra parameterizations which could be fit for Mars and Moon. For Earth, however, Eq. (46) or related equations seem to be appropriate. This can be taken as a confirmation of the Nu – Ra parameterization for the Earth's evolution of Schubert et al. (1979, 1980, 2001).
The other results on non-dimensional numbers are to be found in Section 4.3.

Acknowledgements

We want to thank Woo-Sun Yang for his kind help and interesting discussions. Two of us (U.W. and R.H.) gratefully acknowledge the hospitality of Charles Keller, LANL, Los Alamos, NM. This research was supported by the Volkswagenstiftung through the grant I75474, by the Rechenzentrum der Universität Stuttgart (HLRS), and by the John von Neumann Institute of Computing, Forschungszentrum Jülich, through the supply of computing time.

References

1. Anderson, O.L., 1998. The Grüneisen parameter for iron at outer core conditions and the resulting conductive heat and power in the core. Phys. Earth Planet. Int. 109, 179-197.
2. Barton, M.A. and Stacey, F.D., 1985. The Grüneisen parameter at high pressure: a molecular dynamical study. Phys. Earth Planet. Int. 39, 167-177.
3. Baumgardner, J.R., 1983. A three-dimensional finite element model for mantle convection. Thesis, Univ. of California, Los Angeles.
4. Baumgardner, J.R., 1985. Three-dimensional treatment of convective flow in the Earth's mantle. J. Stat. Phys. 39 (5-6), 501-511.
5. Bercovici, D., 1996. Plate generation in a simple model of lithosphere-mantle flow with dynamic self-lubrication. Earth Planet. Sci. Lett. 144, 41-51
6. Bercovici, D., Ricard, Y., Richards, M.A., 2001a. Relation between mantle dynamics and plate tectonics. In: Richards, M.A., Gordon, R., van der Hilst, R. (Eds.), History and Dynamics of Global Plate Motions. American Geophysical Union, Washington, DC, pp. 5-46
7. Bercovici, D., Ricard, Y., Schubert, G., 2001b. A two-phase model for compaction and damage. 1. General theory. J. Geophys. Res. 106, 8887-8906.
8. Bercovici, D., Ricard, Y., Schubert, G., 2001c. A two-phase model for compaction and damage. 3. Application to shear localization and plate boundary formation. J. Geophys. Res. 106, 8925-8939.
9. Bercovici, D., Ricard, Y. 2002. Energetics of a two-phase model of lithospheric damage, shear localization and plate-boundary formation, Geophys. J. Int., submitted
10. Boehler, R., 1997. The temperature in the Earth's core. In: Crossley, D. J. (Ed.), Earth's Deep Interior. Gordon and Breach Sci. Publ., Amsterdam, pp. 51-63.
11. Braun, M.G., Hirth, G., Parmentier, E.M., 2000. The effects of deep damp melting on mantle flow and melt generation beneath mid-ocean ridges. Earth Planet. Sci. Lett, 176 (3-4), 339-356.
12. Bunge, H.-P., Richards, M.A., Baumgardner, J.R., 1997. A sensitivity study of three-dimensional spherical mantle convection at 10^8 Rayleigh number: effects of depth-dependent viscosity, heating mode, and an endothermic phase change. J. Geophys. Res. 102, 11991-12007.

13. Čadek, O., van den Berg, A.P., 1998. Radial profiles of temperature and viscosity in the Earth's mantle inferred from the geoid and the lateral seismic structure. Earth Planet. Sci. Lett. 164, 607-615.
14. Christensen, U.R., 1984. Heat transport by variable viscosity convection and implications for the Earth's thermal evolution. Phys. Earth Planet. Int. 35, 264-282.
15. Christensen, U.R., 1985. Thermal evolution models for the Earth. J. Geophys. Res. 90, 2995-3007.
16. Christensen, U.R., 1996. The influence of trench migration on slab penetration into the lower mantle. Earth Planet. Sci. Lett. 140, 27-39.
17. Christensen, U.R., Yuen, D.A., 1985. Layered convection induced by phase transitions. J.Geophys. Res. 90, 10291-10300.
18. Chopelas, A., Boehler, R., 1992. Thermal expansivity in the lower mantle. Geophys. Res. Lett. 19, 1983-1986.
19. Čížková, H., Čadek, O., Yuen, D.A., Zhou, H., 1996. Geoid slope spectrum and constraints on mantle viscosity stratification. Geophys. Res. Lett. 23, 3063-3066.
20. Cserepes, L., Yuen, D.A., Schroeder, B.A., 2000. Effect of the mid-mantle viscosity and phase-transition structure on 3D mantle convection. Phys. Earth Planet. Int. 118, 135-148.
21. Dalrymple, G.B., 1991. The Age of the Earth, Stanford University Press, Stanford.
22. Davaille, A., 1999. Simultaneous generation of hotspots and superswells by convection in a heterogeneous planetary mantle. Nature 402, 756-760.
23. Dziewonski, A.M. & Anderson, D.L., 1981. Preliminary reference Earth model. Phys. Earth Planet. Int. 25, 297-356.
24. Forte, A.M., 2000. Seismic-geodynamic constraints of mantle flow: implications for layered convection, mantle viscosity, and seismic anisotropy in the deep mantle. In: Karato, S.-I., Forte, A.M., Liebermann, R.C., Masters, G., Stixrude, L. (Eds.), Earth's Deep Interior. American Geophys. Union, Washington, DC, pp.3-36.
25. Glatzmaier, G.A., 1988. Numerical simulations of mantle convection: Time-dependent, three-dimensional, compressible, spherical shell. Geophys. Astrophys. Fluid Dyn. 43, 223-264.
26. Hofmann, A.W., 1988. Chemical differentiation of the Earth: the relationship between mantle, continental crust, and oceanic crust. Earth Planet. Sci. Lett. 90, 297-314.
27. Howard, L.N., 1966. Convection at high Rayleigh number. In: Grtler, H. (Ed.), Proc. 11th Intl. Congr. Appl. Mech. Springer-Verlag, Berlin, pp.1109-1115.
28. Irvine, R.D. & Stacey, F.D., 1975. Pressure dependence of the thermal Grüneisen parameter, with application to the lower mantle and outer core. Phys. Earth Planet. Int. 11, 157-165.
29. Karato, S.-I., Wang, Z., Liu, B., Fujino, K., 1995. Plastic deformation of garnets: Systematics and implications for the rheology of the mantle transition zone. Earth Planet. Sci. Lett. 130, 13-30.
30. Karato, S.-I., 1997a. Phase transformations and rheological properties of mantle minerals. In: Crossley, D.J. (Ed.), Earth's deep interior: The Doornbos memorial volume. Gordon and Breach Sci. Publ., Amsterdam, pp. 223-272.

31. Karato, S.-I., 1997b. On the separation of crustal component from subducted oceanic lithosphere near the 660km discontinuity. Phys. Earth Planet. Int. 99, 103-111.
32. Karato, S.-I., 2003 Mapping water content in the upper mantle. In preparation.
33. Kenyon, P.M., Turcotte, D.L., 1983. Convection in a two-layer mantle with a strongly temperature-dependent viscosity. J.Geophys. Res. 88, 6403-6414.
34. Kido, M., Čadek, O., 1997. Inferences of viscosity from the oceanic geoid: Indication of a low viscosity zone below the 660-km discontinuity. Earth Planet. Sci. Lett., 151, 125-137.
35. Kido, M., Yuen, D.A., 2000. The role played by a low viscosity zone under a 660km discontinuity in regional mantle layering. Earth Planet. Sci. Lett. 181, 573-583.
36. Kirby, S.H., Stein, S., Okal, E.A., Rubie, D.C., 1996. Metastable mantle phase transformations and deep earthquakes in subducting oceanic lithosphere. Rev. Geophys. 34, 261-306.
37. Kohlstedt, D.L., Evans, B., Mackwell, S.J., 1995. Strength of the lithosphere: Constraints imposed by laboratory experiments. J. Geophys. Res. 100, 17587-17602.
38. Kubo, T., Ohtani, E., Kato, T., Urakawa, S., Suzuki, A., Kanbe, Y., Funakoshi, K., Utsumi, W., Fujino, K., 2000. Formation of metastable assemblages and mechanisms of the grain-size reduction in the post spinel transformation of Mg_2SiO_4. Geophys. Res. Lett. 27, 807-810.
39. Lambeck, K., Johnston, P., 1998. The viscosity of the mantle: Evidence from analyses of glacial-rebound phenomena. In: Jackson, I. (Ed.), The Earth's mantle: Composition, structure and evolution. Cambridge Univ. Press, Cambridge, UK, pp. 461-502.
40. Li, X.D., Romanowicz, B., 1996. Global mantle shear velocity model developed using nonlinear asymptotic coupling theory. J. Geophys. Res. 101, 22245-22272.
41. McCulloch, M.T., Bennett, V.C., 1994. Progressive growth of the Earth's continental crust and depleted mantle: geochemical constraints. Geochim. Cosmochim. Acta 58, 4717-4738.
42. McCulloch, M.T. & Bennett, V.C., 1998. Early differentation of the Earth: an isotopic perspective. In: Jackson, I. (Ed.), The Earth's mantle. Cambridge Univ. Press, Cambridge, pp.127-158.
43. O'Neill, H.S.C., Palme, H., 1998. Composition of the silicate Earth: implications for accretion and core formation. In: Jackson, I. (Ed.), The Earth's Mantle. Cambridge Univ. Press, Cambridge, pp. 3-126.
44. Pari, G., Peltier, W.R., 1998. Global surface heat flux anomalies from seismic tomography-based models of mantle flow: Implications for mantle convection. J.Geophys. Res. 103, 23743-23780.
45. Parsons, B., McKenzie, D., 1978. Mantle convection and the thermal structure of the plates. J. Geophys. Res. 83, 4485-4496.
46. Pollack, H.N., Hurter, S.J., Johnson, J.R., 1993. Heat flow from the Earth's interior: analysis of the global data set. Rev. Geophys. 31, 267-280.
47. Ranalli, G., 1998. Inferences on mantle rheology from creep laws. GeoResearch Forum 3-4, 323-340.

48. Rattcliff, J.T., Tackley, P.J., Schubert, G., Zebib, A., 1997. Transitions in thermal convection with strongly variable viscosity. Phys. Earth Planet. Int. 102, 201-212.
49. Reese, C.C., Solomatov, V.S., Moresi, L.-N., 1998. Heat transport efficiency for stagnant lid convection with dislocation viscosity: Application to Mars and Venus. J. Geophys. Res. 103, 13643-13657.
50. Reese, C.C., Solomatov, V.S., Moresi, L.-N., 1999. Non-Newtonian stagnant lid convection and magmatic resurfacing on Venus. Icarus 139, 67-80.
51. Ricard, Y., Bercovici, D., Schubert, G., 2001. A two-phase model for compaction and damage. 2. Applications to compaction, deformation and the role of interfacial surface tension. J. Geophys. Res. 106, 8907-8924.
52. Richards, M.A., Yang, W.-S., Baumgardner, J.R., Bunge, H.-P., 2001. Role of a low-viscosity zone in stabilizing plate tectonics: Implications for comparative terrestrial planetology. Geochemistry, Geophysics, Geosystems vol. 2, paper no.2000GC000115
53. Richter, F.M., 1973. Finite amplitude convection through a phase boundary. Geophys. J. R. Astron. Soc. 35, 265-276.
54. Ringwood, A.E., 1990. Slab-mantle interactions: petrogenesis of intraplate magmas and structure of the upper mantle. Chem. Geol. 82, 187-207.
55. Schubert, G., Cassen, P., Young, R.E., 1979. Subsolidus convective cooling histories of terrestrial planets. Icarus 38, 192-211.
56. Schubert, G., Stevenson, D., Cassen, P., 1980. Whole planet cooling and the radiogenic heat source contents of the Earth and Moon. J. Geophys. Res. 85, 2511-2518.
57. Schubert, G., Turcotte, D.L., Olson, P., 2001. Mantle Convection in the Earth and Planets. Cambridge Univ. Press, Cambridge, 940 pp.
58. Sleep, N.H., 1979. Thermal history and degassing of the Earth: Some simple calculations. J. Geology 87, 671-686.
59. Solomatov, V.S., 1995. Scaling of temperature- and stress-dependent viscosity convection. Phys. Fluids 7, 266-274.
60. Spada, G., Sabadini, R., Yuen, D.A., Ricard, Y., 1992. Effects on postglacial rebound from the hard rheology in the transition zone. Geophys. J. Int. 109, 683-700.
61. Stacey, F.D., 1992. Physics of the Earth, 3rd edn., Brookfield Press, Brisbane, 513 pp.
62. Stacey, F.D., 1996. Thermoelasticity of (Mg,Fe)SiO_3 perovskite and a comparison with the lower mantle. Phys. Earth Planet. Int. 98, 65-77.
63. Stacey, F.D., 1998. Thermoelasticity of a mineral composite and a reconsideration of lower mantle properties. Phys. Earth Planet. Int. 106, 219-236.
64. Stacey, F.D., Stacey, C.H.B., 1999. Gravitational energy of core evolution: implications for thermal history and geodynamo power. Phys. Earth Planet. Int. 110, 83-93.
65. Stevenson, D.J., Spohn, T., Schubert, G., 1983. Magnetism and thermal evolution of the terrestrial planets. Icarus 54, 466-489.
66. Tackley, P.J., 1997. Effects of phase transitions on three-dimensional mantle convection. In: Crossley, D.J. (Ed.), Earth's deep interior: the Doornbos memorial volume. Gordon and Breach Sci. Publ., Amsterdam, pp. 273-335.

67. Tackley, P.J., 2000a. Self-consistent generation of tectonic plates in time-dependent, three-dimensional mantle convection simulations. 1. Pseudo-plastic yielding. Geochem. Geophys. Geosyst., 1, Paper no. 2000GC000036
68. Tackley, P.J., 2000b. Self-consistent generation of tectonic plates in time-dependent, three-dimensional mantle convection simulations. 2. Strain weakening and asthenosphere. Geochem. Geophys. Geosyst., 1, Paper no. 2000GC000043
69. Tackley, P.J., 2001. The quest for self-consistent generation of plate tectonics in mantle convection models. In: Richards, M.A., Gordon, R., van der Hilst, R. (Eds.), History and Dynamics of Global Plate Motions. American Geophysical Union, Washington, DC, pp. 47-72
70. Trompert, R., Hansen, U., 1998. Mantle convection simulations with rheologies that generate plate-like behavior. Nature 395, 686-689.
71. van den Berg, A.P. & Yuen, D.A., 1998. Modelling planetary dynamics by using the temperature at the core-mantle boundary as a control variable: effect of rheological layering on mantle heat transport. Phys. Earth Planet. Int. 108, 219-234.
72. van der Hilst, R.D.; Widiyantoro, S., Engdahl E.R., 1997. Evidence for deep mantle circulation from global tomography. Nature 386, 578-584
73. van der Hilst, R.D., Kárason, H., 1999. Compositional Heterogeneity in the Bottom 1000 Kilometers of Earth's Mantle: Toward a Hybrid Convection Model. Science 283, 1885-1888.
74. Walzer. U., Hendel, R., 1999. A new convection-fractionation model for the evolution of the principal geochemical reservoirs of the Earth's mantle. Phys. Earth Planet. Int. 112, 211-256.
75. Walzer, U., Hendel, R., 2003. Chemical differentiation, viscosity and the thermal evolution of the mantle. In preparation.
76. Weidner, D.J., Chen, J., Xu,Y., Wu,Y., Vaughan,M.T., Li,L., 2001. Subduction zone rheology. Phys. Earth Planet. Int. 127,67-81.
77. Yang, W.-S., 1997. Variable viscosity thermal convection at infinite Prandtl number in a thick spherical shell. Thesis, Univ. of Illinois, Urbana-Champaign.
78. Zerr, A. & Boehler, R., 1993. Melting of (Mg,Fe)SiO_3-perovskite to 625 kilobars: indication of a high melting temperature in the lower mantle. Science 262, 553-555.
79. Zerr, A. & Boehler, R., 1994. Constraints on the melting temperature of the lower mantle from high-pressure experiments on MgO and magnesiowstite. Nature 371, 506-508.
80. Zhang, S., Yuen, D.A., 1996. Intense local toroidal motion generated by variable viscosity compressible convection in 3-D spherical-shell. Geophys. Res. Lett. 23, 3135-3138.